Geomorphology 182 (2013) 49–65

Contents lists available at SciVerse ScienceDirect

Geomorphology

journal homepage: www.elsevier.com/locate/geomorph

Nature and timing of large landslides within an active orogen, eastern Pamir, China

Zhaode Yuan [a,b], Jie Chen [a,*], Lewis A. Owen [c], Kathryn A. Hedrick [c], Marc W. Caffee [d], Wenqiao Li [a], Lindsay M. Schoenbohm [e], Alexander C. Robinson [f]

[a] State Key Laboratory of Earthquake Dynamics, Institute of Geology, China Earthquake Administration, Beijing 100029, China
[b] China Earthquake Disaster Prevention Center, Beijing 100029, China
[c] Department of Geology, University of Cincinnati, Cincinnati, OH 45221, USA
[d] Department of Physics/PRIME Laboratory, Purdue University, West Lafayette, IN 47906, USA
[e] Department of Chemical and Physical Sciences, University of Toronto Mississauga, Mississauga, Canada ON L5L 1C6
[f] Department of Earth and Atmospheric Sciences, University of Houston, Houston, TX 77204-5007, USA

ARTICLE INFO

Article history:
Received 18 June 2012
Received in revised form 26 October 2012
Accepted 26 October 2012
Available online 12 November 2012

Keywords:
Landslides
Be-10
Cosmogenic nuclide dating
China
Tibet
Pamir

ABSTRACT

Large-scale landsliding (involving $\gg 10^6$ m^3 in volume) is important in landscape development in high mountains. To assess the importance of large landslides in high mountains, four large landslides (Bulunkou, Muztagh, Taheman, and Yimake) were mapped in the NE Chinese Pamir at the westernmost end of the Himalayan–Tibetan orogen and dated using ^{10}Be terrestrial cosmogenic nuclides. The Bulunkou landslide at the southernmost end of Muji Valley is composed of ~1.7×10^7 m^3 of landslide debris and has an age of 2.0 ± 0.1 ka. The Muztagh landslide, located on the SW side of the massif Muztagh Ata, is composed of ~4.7×10^8 m^3 of debris, and has an age of 14.3 ± 0.8 ka. The Taheman landslide, located south of Muztagh Ata, is composed of ~2.6×10^8 m^3 of landslide debris and has an age of 6.8 ± 0.2 ka. The Yimake landslide, on the northern frontal range of the Pamir at the southwestern end of the Tarim basin, is composed of ~1.4×10^9 m^3 of landslide debris and has an age of 7.1 ± 0.6 ka. Two other large landslides are present in the region, the Aerpa Aigezi (on a tributary of the Gez River) and the Bile Jiyi (on the Yarkand River) landslides, and are composed of ~1.6×10^7 m^3 and ~5.2×10^6 m^3 of landslide debris, respectively. However, the Aerpa Aigezi and Bile Jiyi landslides were not studied in as much detail or dated because of their inaccessibility. Given the tectonically active nature of this region, with numerous active faults, and the morphology of the landslides, these landslides were likely triggered by earthquakes. However, other causes — including long-term increased precipitation and geologic bedrock structure — could be important contributing factors in their formation.

1. Introduction

Large-scale landslides/rock avalanches exceeding $>10^6$ m^3 of landslide debris are significant agents of erosional degradation in mountains and changes in orogenic mass balance, and also imperil human populations and their infrastructure (Dortch et al., 2009; Korup and Clague, 2009; Shroder et al., 2011). Determining the distribution of landslides through time is key to assessing hazards and for understanding triggering mechanisms — such as climatic change, phases of enhanced earthquake activity, and/or post-glacial stress relaxation — and for developing models for landscape evolution. However, few studies have been undertaken on large landslides in the high mountains of central Asia because of the logistical and political inaccessibility of the region and associated problems of mapping and sampling for numerical dating. Dortch et al. (2009) provided a comprehensive review of dated large landslides in the Himalayan–Tibetan orogen. We build on this study by examining and dating, using ^{10}Be terrestrial cosmogenic nuclides (TCN), large landslides in the eastern Chinese Pamir (Fig. 1). We then compare large landslides of known age in the region to explore possible temporal correlations and discuss importance of large landslides in landscape development.

2. Regional setting

The study area is situated in the Pamir at the western end of the Himalayan–Tibetan orogen (Fig. 1). The northern margin of the Pamir was thrust northward by ~300 km during the late Cenozoic (Burtman and Molnar, 1993). Active deformation in the eastern Pamir is dominated by east–west extension along the 250-km-long Kongur Shan extensional system (Arnaud et al., 1993; Brunel et al., 1994; Robinson et al., 2004).

* Corresponding author. Tel./fax: +86 10 62009093.
E-mail address: chenjie@ies.ac.cn (J. Chen).

0169-555X/$ – see front matter © 2012 Elsevier B.V. All rights reserved.
http://dx.doi.org/10.1016/j.geomorph.2012.10.028

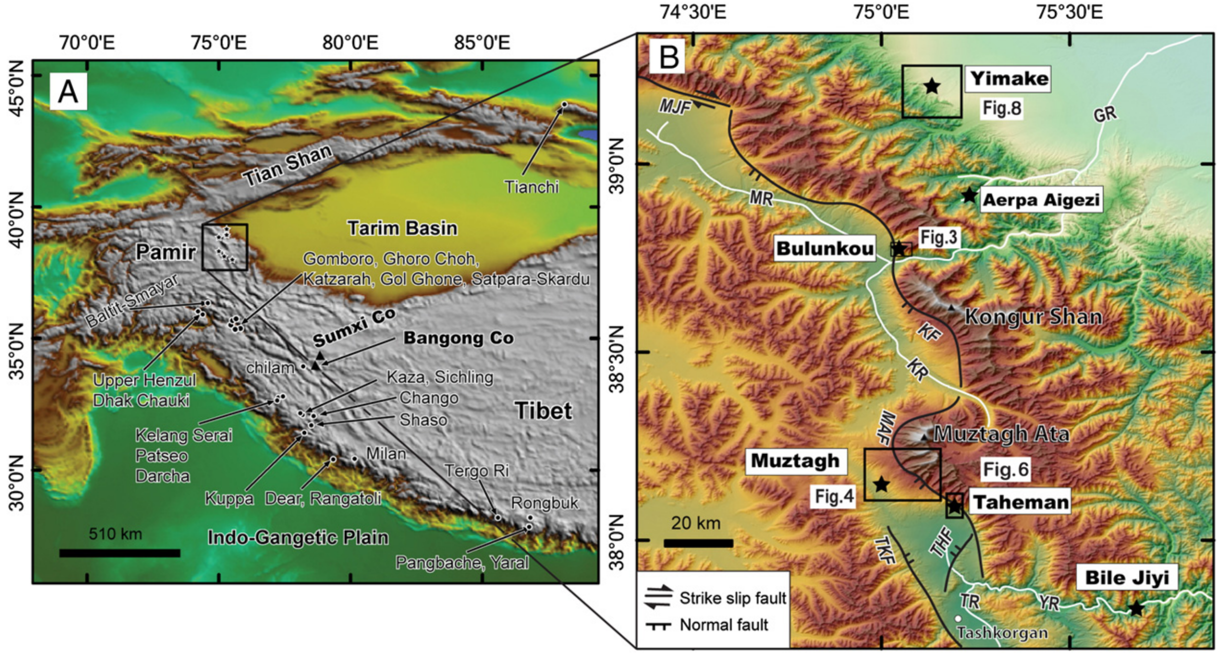

Fig. 1. Locations of landslides examined in this study (stars) and previously dated landslides of Dortch et al. (2009) (dots). (A) SRTM DEM of the western part of the Tibetan–Himalayan orogen. (B) ASTER DEM of the detailed study areas showing the location of the landslide case studies examined in this paper. MJF — Muji Fault; KF — Kongur Shan Fault; MAF — Muztagh Ata Fault; TKF — Tashkorgan Fault; THF — Taheman Fault; MR — Muji River; GR — Gez River; KR — Kangxiwa River; TR — Tashkorgan River; YR — Yarkand River.

Along the eastern Pamir, the topography rises from ~1200 m above sea level (asl) in the Tarim basin to peaks exceeding 7000 m asl. The major rivers that drain the high topography in region are the Gez River, including its tributaries the Muji River and Kangxiwa River; and the Tashkorgan River, a tributary to the Yarkand River (Fig. 1B).

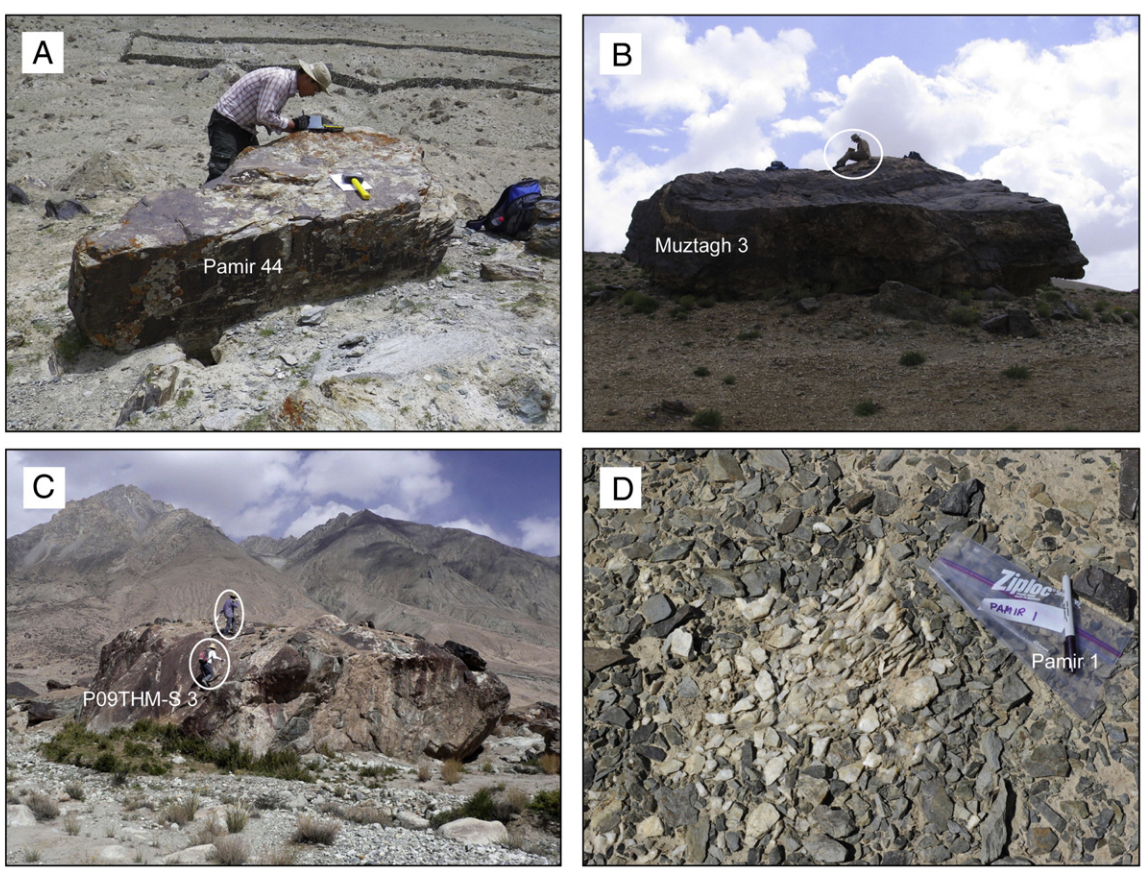

Fig. 2. View of typical boulders sampled for ^{10}Be surface exposure dating on the (A) Bulunkou, (B) Muztagh, (C) Taheman, and (D) Yimake landslides. Sample numbers are shown on the blocks or plastic bag. The ellipses enclose people for scale.

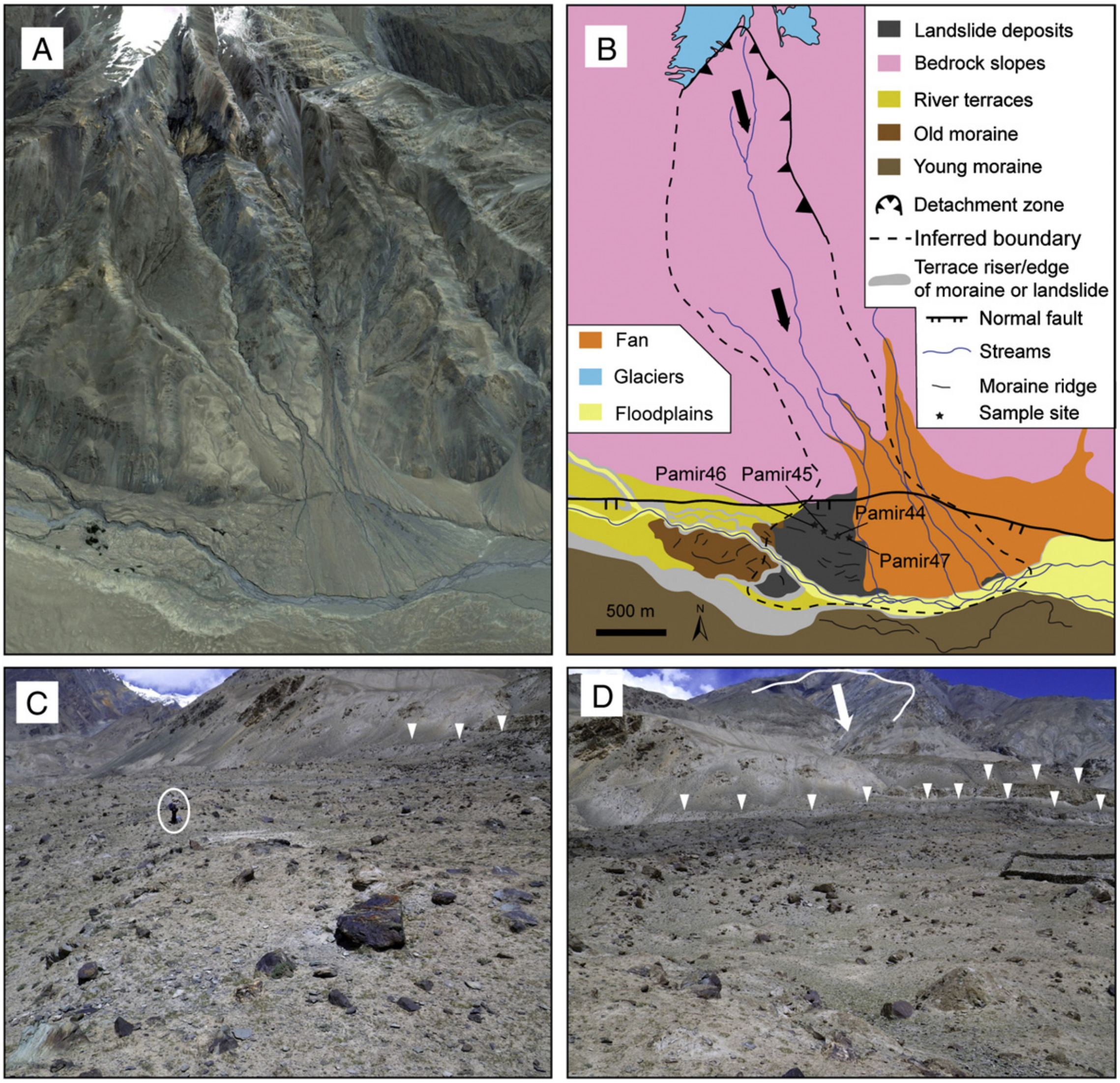

Fig. 3. The Bulunkou landslide. (A) Google Earth image showing the landslide. (B) Interpretation of the image showing Holocene active normal fault across the landslide. (C) looking north showing landslide debris and (D) looking east across the landslide to its scar (white arrow). White downward pointing triangles indicate the locations of fault scarp and the ellipse encloses a person for scale.

Climatologically, the NE Pamir is an arid region dominantly influenced by mid-latitude westerlies, as well as the Indian summer monsoon. In the NE Pamir, from 1971 through 2000, the average annual temperature was 3.6 °C with a mean annual precipitation of 68.1 mm (Sun et al., 2006). Most precipitation occurs in spring (~22%) and summer (~54%) (Sun et al., 2006) with the summer precipitation most likely associated with the south Asian monsoon (Seong et al., 2009c).

The glacial history of NE Pamir is relatively well studied. Three main glacial stages are recognized around Muztagh Ata: from oldest to youngest these are the Karasu glacial stage (a glaciation prior to the penultimate glacial cycle); the Subaxh glacial stage (the penultimate glacial cycle and/or the last glacial cycle); and the Olimde glacial stage (from a few hundred years to 17.1 ± 0.3 ka) (Seong et al., 2009b). In the Tashkurgan Valley, just south of our study area, Owen et al. (2012) assigned moraines to four glacial stages: the Dabudaer glacial stage (the penultimate glacial cycle or earlier); the Tashkurgan glacial stage (Marine Oxygen Isotope Stage [MIS] 4); the Hangdi glacial stage (MIS2); and the Kuzigan glacial stage (Last Glacial Maximum).

3. Methods

3.1. Landslide mapping

Landslides are difficult to identify in the Himalayan–Tibetan orogen because extreme fluvial and glacial erosion often destroys the diagnostic morphologies (Owen, 1991; Hewitt, 1999; Hewitt et al., 2011), and the original diamictions that constitute landslides and glacial deposits look very similar and can be easily misidentified (Owen, 1991). Careful and detailed landslide mapping was done in the field using the criteria highlighted in Hewitt (1999) to distinguish between landslide and glacial deposits. The sheer size of large landslides makes it relatively easy to identify them in our study area. Four large landslides were identified in the field and studied in detail: the Bulunkou, Muztagh, Taheman, and Yimake landslides (Fig. 1). They were mapped with support of high resolution Google Earth imagery and 3 arc-sec (~90 m) Shuttle Radar Topography Mission (SRTM) digital elevation models (DEMs). We first present basic geomorphic details and TCN dating for the Taheman landslide in Yuan et al. (2012), which was published in Chinese.

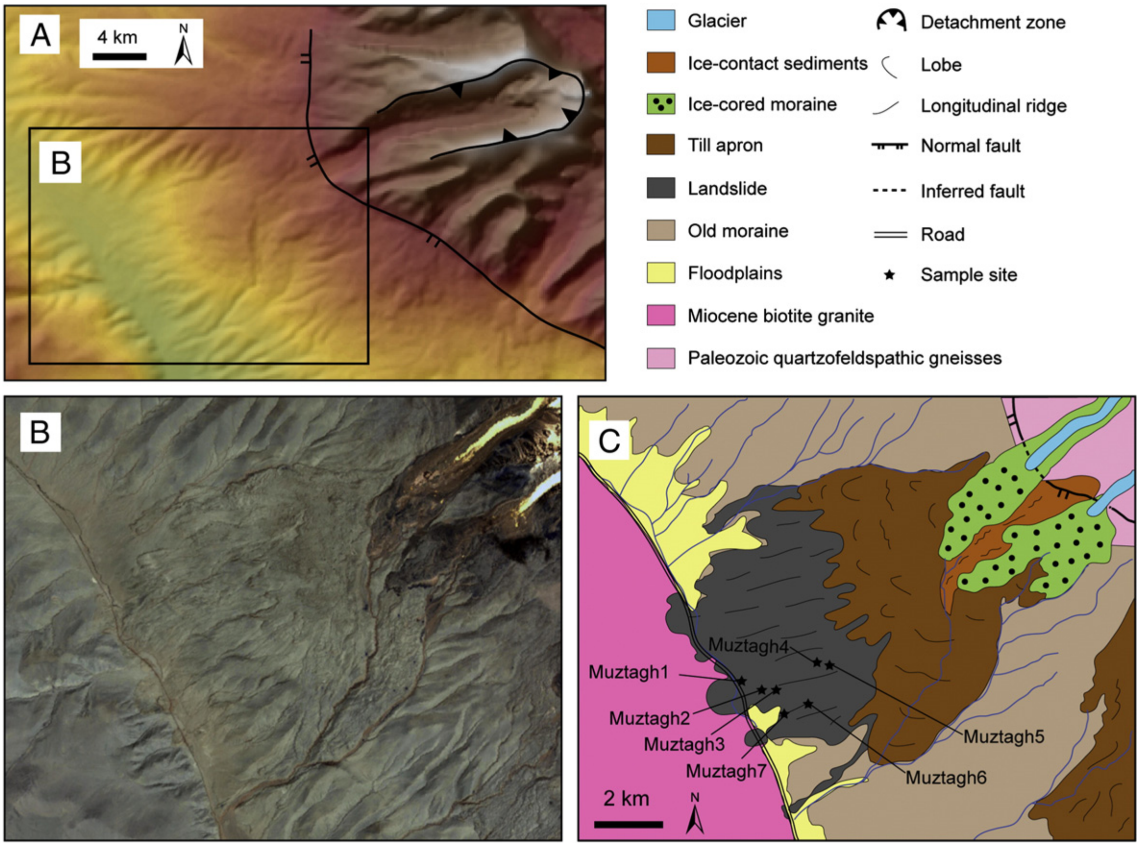

Fig. 4. (A) SRTM DEM of the Muztagh landslide showing U shaped detachment zone modified by glaciers. (B) False-color ASTER image of Muztagh landslide deposit and (C) its interpretation, modified from Seong et al. (2009c).

The geomorphic details and dating are presented again in this manuscript to provide a comprehensive and more accessible account of this large landslide and for easy comparison with our other studies of large landslides in the Pamir. We used Google Earth and SRTM DEMs to examine an area of ~27,700 km^2 in the Chinese Pamir (Fig. 1). Only two other large landslides, the Aerpa Aigezi and the Bile Jiyi landslides, named after nearby villages, were identified. We were not able to date these landslides or study them in great detail because of their inaccessibility.

3.2. Sampling for terrestrial cosmogenic nuclide surface exposure dating

Large quartz-rich boulders on the surface of the Bulunkou, Muztagh, and Taheman landslide deposits, and ~1 kg of disintegrated quartz boulders and quartz clasts on the Yimake landslide deposit were sampled for ^{10}Be surface exposure dating (Fig. 2). About 500 g of rock sample was collected from the upper surface of each sampled boulder to a depth of <5 cm. Four to seven boulders were sampled on each landslide deposit to provide a check on the reproducibility of the dates and an assessment of possible prior exposure (inherited TCNs), weathering, exhumation, or toppling of boulders that might have occurred. The large boulders on the Yimake landslide deposit were composed of chlorite schist and limestone, a lithology that is not suitable for ^{10}Be dating, so we collected quartz pebbles eroded from quartz veins in boulders and disintegrated quartz boulders (Fig. 2D). Each boulder was photographed, its dimensions measured, and the degree of weathering and the site characteristics were recorded. The inclination from the sampling site to the tops of surrounding mountain ridges or peaks was measured as a function of azimuth to determine the topographic shielding. The strike and dip direction of the sampling boulder surface were also measured if the sampled surface was not horizontal.

3.3. Laboratory methods for terrestrial cosmogenic nuclide surface exposure dating

Rock samples were crushed and sieved to obtain a 250–500 μm size fraction which then was chemically leached using acid leaches: aqua regia for >9 h; one or more 5% HF/HNO_3 leaches for ~24 h; and one or more 1% HF/HNO_3 leaches, each for ~24 h. A heavy liquid (lithium heteropolytungstate) separation was used after the 5% HF/HNO_3 leach. The purity of the quartz separate was tested using an optical microscope or using infrared stimulated luminescence in a Riso OSL Reader. The obtained pure quartz was spiked with a Be carrier having a $^{10}Be/^{9}Be$ ratio of $3.9 \pm 0.8 \times 10^{-15}$ for the Muztagh and Taheman samples, $9.7 \pm 1.8 \times 10^{-15}$ for the Yimake samples, and $7.3 \pm 1.0 \times 10^{-15}$ for the Bulunkou samples. The spiked quartz was dissolved in concentrated HF and then fumed three times with perchloric acid. Samples were then passed through anion and cation exchange columns to separate the Be fraction. Ammonium hydroxide was added to the Be fractions to precipitate $Be(OH)_2$ gel, which was calcinated by ignition at 750 °C for 5 min in quartz crucibles. The resultant BeO was mixed with Nb powder and loaded into steel targets for the measurement of the $^{10}Be/^{9}Be$ ratios by accelerator mass spectrometry at PRIME Laboratory in Purdue University.

All ^{10}Be TCN ages for boulder samples were calculated using the CRONUS Earth 2.2 calculator (Balco et al., 2008; http://hess.ess.washington.edu/math/), with a production rate of 4.49 ± 0.39 ^{10}Be atoms/g of quartz/y, a ^{10}Be half-life of 1.36×10^6 years (Nishiizumi et al., 2007); and using a rock density of 2.75 g/cm^3

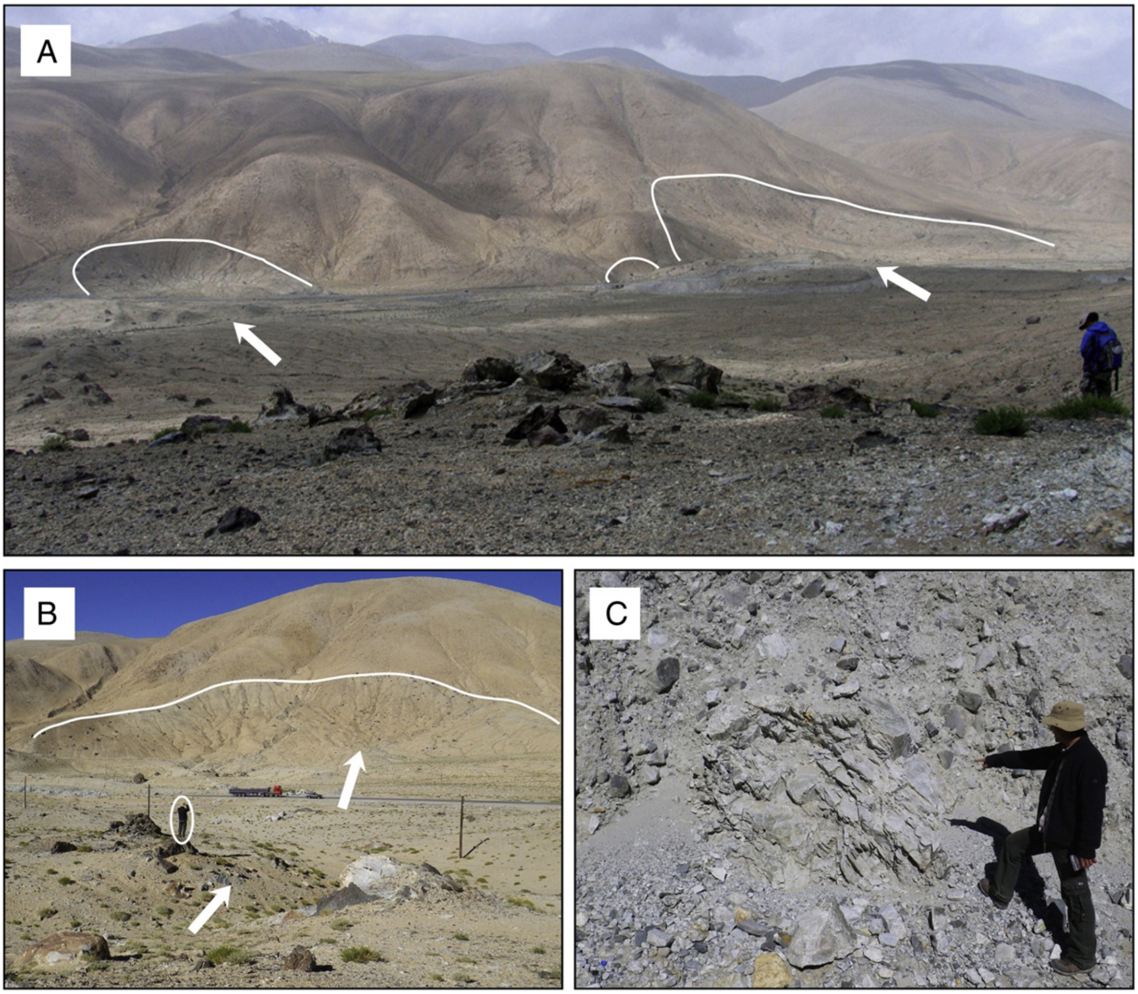

Fig. 5. The Muztagh landslide. (A) View west at the top of the landslide showing the landslide debris, which is present up to ~120 m above the valley floor on the opposite hill from the landslide scar and (B) the right toe in the landslide debris shown in (A). (C) A boulder within the landslide deposit in the roadcut showing jigsaw texture. The white arrows show the direction that the landslide advanced.

and zero erosion. Owen et al. (2012) estimated the erosion rate in Tashkurgan Valley to be ~2.3 m/Ma. If our samples were weathered at this rate of 2.3 m/Ma, then an age of 1 ka would be underestimated by ~0.2%, a 10 ka age by ~2%, a 20 ka age by ~4%, a 40 ka age by ~9%, a 100 ka by ~28%, and a 200 ka by ~122%. We argue that the boulders we sampled on the Bulunkou, Muztagh, and Taheman landslides experienced minimal weathering and that 2.3 m/Ma erosion is a maximum erosion rate for our study areas. The samples collected on the Yimake landslide have a higher degree of weathering so the ^{10}Be ages are minimum ages.

4. Landslide descriptions

4.1. Bulunkou landslide

The Bulunkou landslide is located north of the town of Bulunkou at the southernmost end of Muji Valley (Fig. 1). The landslide scar is on a SW-facing slope at an altitude of between ~4500 and ~5100 m asl and has an area of 8.6×10^5 m^2. The surface of the scar is parallel or subparallel to strike of foliation in the bedrock that is composed of quartzofeldspathic gneisses (Robinson et al., 2004; Fig. 3A).

The Bulunkou landslide deposit covers an area of ~1.7×10^6 m^2, including the buried part. We calculated the total area of the deposit by assuming that the original deposit has a lobe shape. Large alluvial fan deposits overlie part of the landslides, making it difficult to determine the exact extent of its deposit (Fig. 3). Determining the thickness of the deposit is difficult, but individual hummocks rise about 15–20 m above the surrounding topography. The Bulunkou landslide is vertically offset by ~9 m by the Kongur Shan normal fault, revealing that the landslide deposit is >9 m thick (Fig. 3C). The toe of the landslide likely blocked a tributary to the Muji River and was subsequently incised to produce an impressive cliff that is 5–10 m high. Thus, part of the original volume of the landslide has been removed by erosion. As a conservative estimate, we assume that the landslide deposit has an average thickness of ~10 m, so its volume is $>1.7\times10^7$ m^3. Very angular large (>1 m in diameter) boulders are abundant on the surface of the landslide. Some of boulders are highly weathered with deep pits (>10 mm) and caverns (cm-deep). Unweathered boulders were difficult to find, but we were able to sample four boulders (Pamir 44–47) for ^{10}Be dating that exhibited little weathering.

4.2. Muztagh landslide

The Muztagh landslide is located on the SW side of the Muztagh Ata massif and has been previously described by Fort and Peulvast (1995) and Seong et al. (2009c). Fort and Peulvast (1995) interpreted the deposit as an avalanche-debris flow and considered its kettle-like

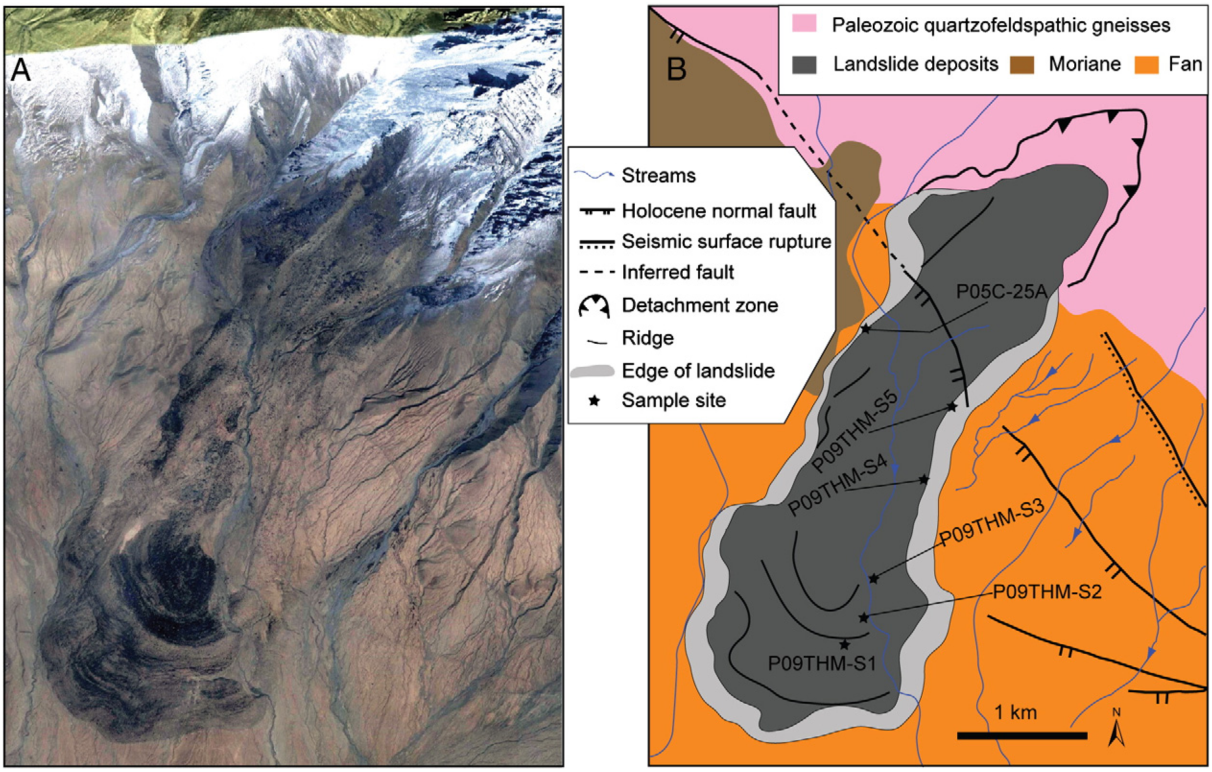

Fig. 6. The Taheman landslide. (A) Google Earth image of the landslide and (B) a simplified geomorphic map showing the landslide lobes and active faults (adapted from Yuan et al., 2012).

surficial morphology as indicative of mass movement processes with debris incorporating rock and ice.

The landslide scar was modified and overridden by a glacier to produce its current U-shaped form (Fig. 4A). Bedrock foliations dip SW21° in average around the U-shaped valley. The Olimde glacial stage moraine of Seong et al. (2009c) overlies parts of the landslide deposit (Fig. 4B and C). The landslide deposit is composed of Triassic quartzofeldspathic gneisses (Robinson et al., 2012) and has an area of ~4.7×10^7 m^2, including the part buried by moraine. A roadside exposure reveals that the landslide deposit is at least 10 m thick, providing an estimated minimum volume of ~4.7×10^8 m^3. The landslide debris comprises several separate lobes that stretch across the valley and up the opposite valley wall to a vertical height of ~120 m (Fig. 5A and B). Some boulders on the surface are larger than 9 m in length (Fig. 2B), and some are cracked and form jigsaw pieces (centimeter-size fractures separating boulders into several pieces that still fit together) (Fig. 5C). Holocene fault scarps are present to the north and the south of the landslide along the mountain front of Muztagh Ata (Fig. 4A and C).

4.3. Taheman landslide

The Taheman landslide is located to the south of Muztagh Ata (Fig. 6). Seong et al. (2009c) described this landslide and suggested that the 1895 Tashkorgan earthquake (M7) triggered its formation. However, Yuan et al. (2012) were able to demonstrate using ^{10}Be TCN dating that the Taheman landslide formed during the early Holocene. Yuan et al. (2012) show that the landslide scar is triangular and has an area of ~4.6×10^5 m^2 (Fig. 7A) and that the bedrock is gneisses, and foliation dips ~60° SW in the same direction as the landslide runout path. The landslide debris forms large (hundreds of meters long) longitudinal and transverse ridges (Fig. 6). The deposit has an area of 5.1×10^6 m^2; and its margin rises ~50 m above the surrounding landscape, indicating a volume of ~2.6×10^8 m^3. This revises our estimate of 155×10^6 m^3 that is presented in Yuan et al. (2012). The landslide is incised by an active stream, which provides good exposures through the deposits (Fig. 7B). The surface boulders are very angular and range up to 20 m in diameter (Fig. 2C). A Holocene normal fault displaces the landslide to form a 10–15 m high scarp (Figs. 6B and 7A).

4.4. Yimake landslide

The Yimake landslide is located along the northern frontal range of the Pamir and has an area of ~4.8×10^7 m^2 with a hummocky surface (Figs. 8 and 9). The thickness of the landslide's eastern edge is ~29 m, which is a mean value we measured using a TruPulse 200 Rangefinder at five different sites along the eastern edge, which provides a volume of ~1.4×10^9 m^3. The headscarp consists of three small separate headscarps dipping NE (Figs. 8 and 9A). The distance from the headscarp to the foremost margin is ~15 km.

The bedrock in the source area is comprised of chlorite schist and limestone and has several sets of joints (Fig. 9C and D). The bedding dips 15–40° SW (1:200,000 Chinese geology map), but the direction of mass movement is NE. No active fault crosses the landslide. The eastern margin shows two layers (Fig. 9E), and farther north of the station shown in Fig. 9E the landslide deposits overlie fluvial pebble deposits (Fig. 9F), suggesting that the huge amount of debris is not moraine but landslide deposits.

4.5. Aerpa Aigezi and Bile Jiyi landslides

The Aerpa Aigezi landslide is located near Aerpa-Aigezi village, which is part of the Aoyi-Take township. The landslide debris covers an area of ~6.2×10^5 m^2 (Figs. 1 and 10). As determined using Google Earth, the thickness of the landslide along its eastern edge is ~26 m

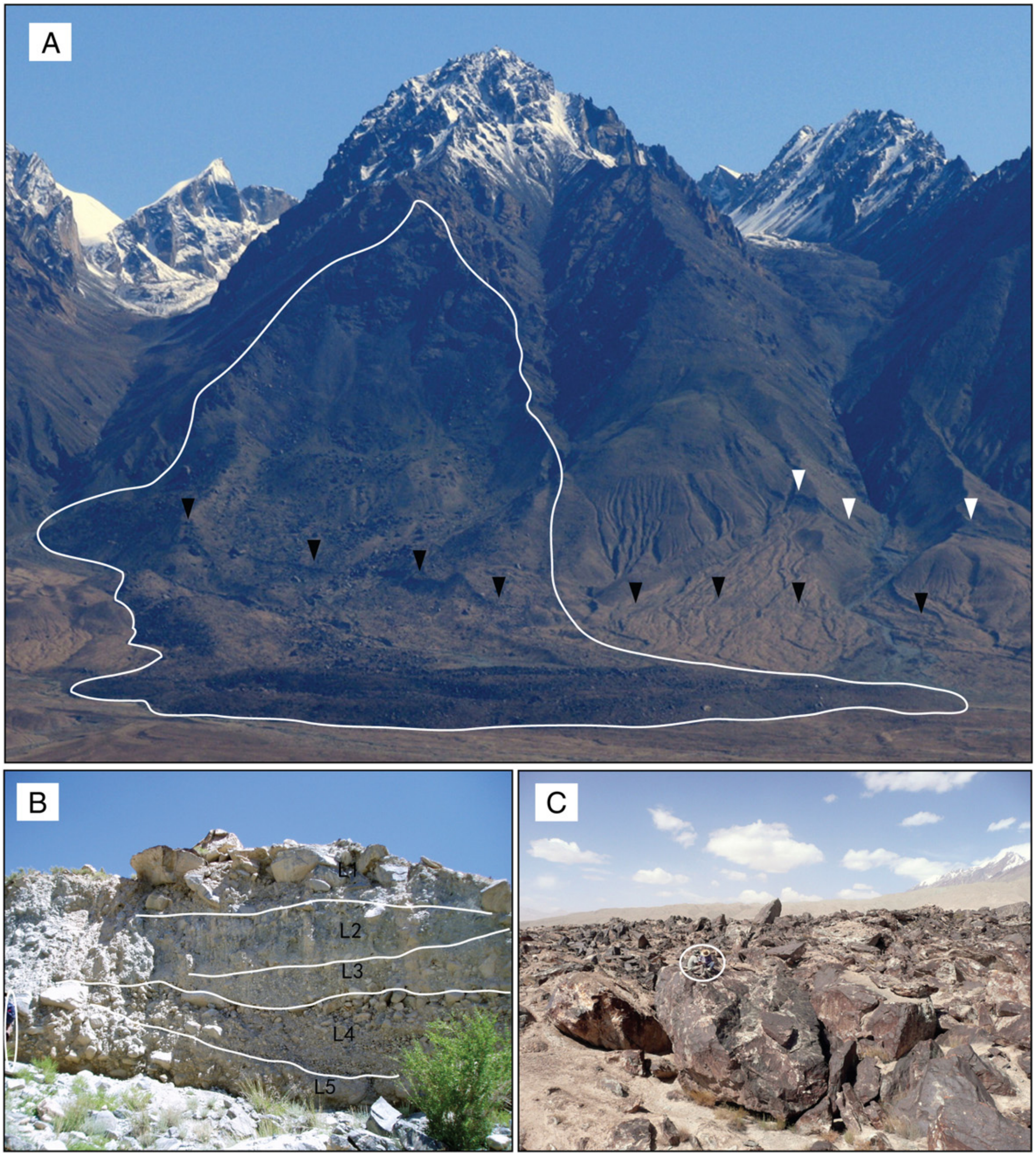

Fig. 7. The Taheman landslide. (A) View northeast from national highway G314 showing a clear triangular landslide scar. Black and white downward pointing triangles indicate the locations of fault scarp and 1895 earthquake surface rupture, respectively. (B) East view of stream exposure with the landslide debris showing stratified diamict. The white ellipse encloses a person for scale. (C) View northwest of landslide surface showing many large, angular blocks. The white circle encloses two people for scale.

calculated through getting several elevation points on landslide east edge surface and its close floodplain surface respectively, suggesting a volume of ~1.6×10^7 m^3. The landslide dammed a tributary to Gez River but is now cut through. Google Earth images show that the landslide height from the riverbed to the top of the scar is ~770 m. The front of the landslide climbed ~100 m up the opposite hillslope. The bedrock at this location is Devonian metagraywacke (Robinson et al., 2007).

The Bile Jiyi landslide is ~60 km east of Tashkorgan County. Its debris covers an area of ~2.6×10^5 m^2 and is very evident on Google Earth images (Figs. 1 and 11A). Measured using Google Earth, the landslide height from the riverbed to the top of the scar is ~930 m, and the front of the landslide advanced ~80 m up the opposite hillslope. A ~20-m-thick deposit of lake sediments on top of the landslide deposits shows that the landslide dammed the Yarkand River (Fig. 11). As the thickness of the landslide deposits should be more than the thickness of the lacustrine deposits, the total volume of deposits is at least 5.2×10^6 m^3. The landslide deposits are quartzofeldspathic gneisses.

5. Dating results

The ^{10}Be ages for the four landslides are presented in Fig. 12 and Table 1. The ^{10}Be ages for these four landslides and recalculated published ^{10}Be ages of other landslides in the Himalayan–Tibetan orogen are presented in Tables 2 and 3. Ages for Uhen II, Patseo-6,

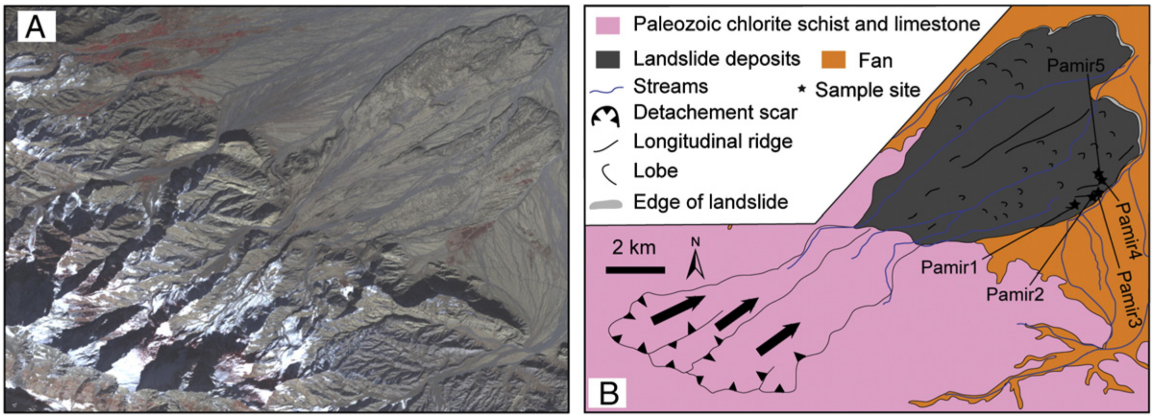

Fig. 8. False-color ASTER image of Yimake landslide deposit (A) and a geomorphic map summarizing its main features (B).

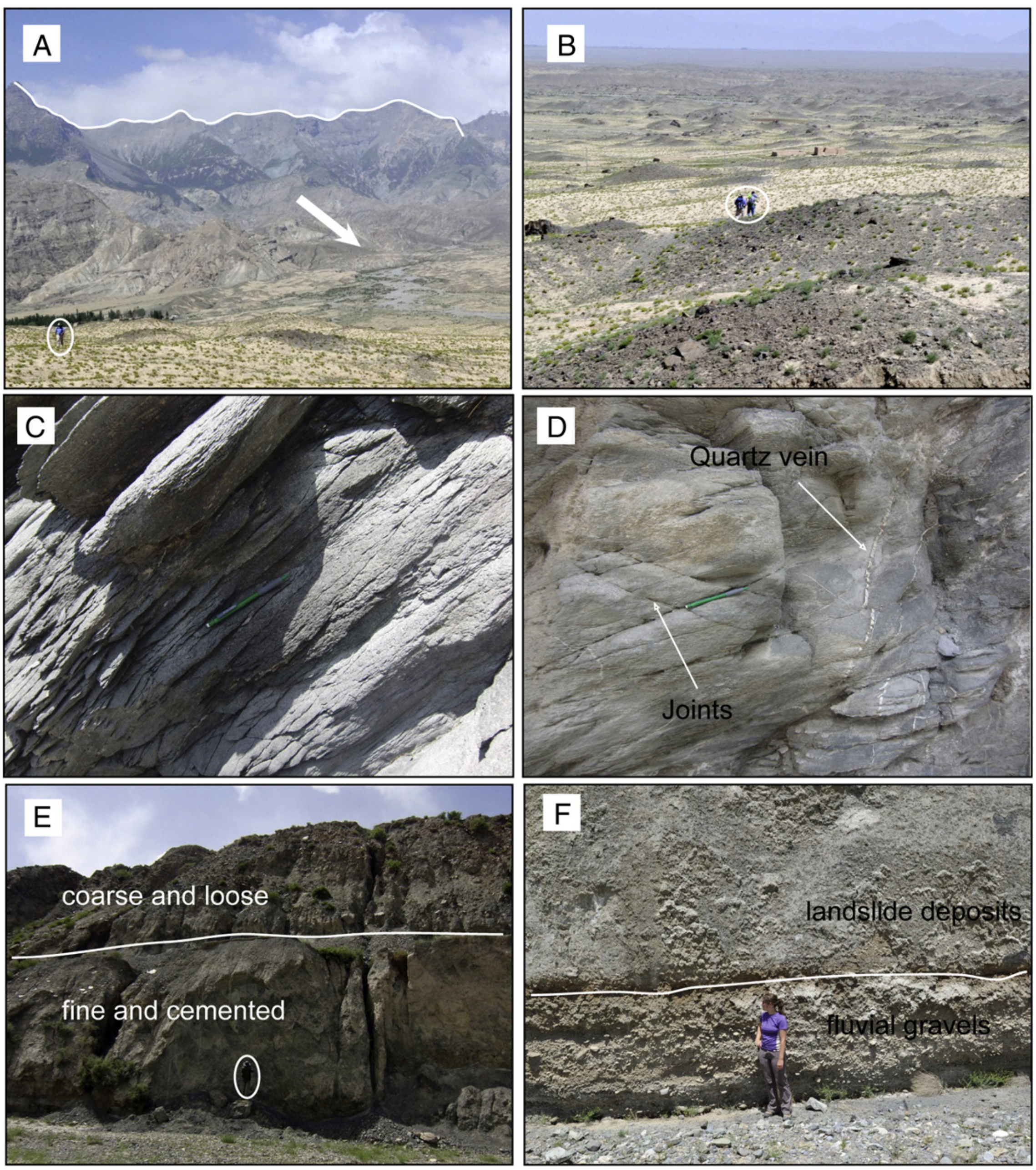

Fig. 9. The Yimake landslide on the northern margin of Pamir. (A) View southwest showing the landslide scar. (B) View north showing hummocks on the landslide surface. (C) Bedrock foliation. (D) Bedrock joints and quartz veins. (E) East margin of the landslide showing two units of landslide deposits. (F) Landslide deposits overlying fluvial gravels. The ellipses enclose people for scale.

Fig. 10. Google Earth image of Aerpa Aigezi landslide showing debris accumulated on the hill opposite the landslide. Black arrows show the direction that the landslide advanced.

E110, TCB-2, TCB-7, and KTM11 samples (Table 2) were not considered in the mean age calculations as they lie beyond 3σ of the mean of the set of dates for their landforms. Mean ages for Bulunkou, Muztagh, Taheman, and Yimake are 2.0 ± 0.1 ka (uncertainty = 1 σ; $n = 4$), 14.3 ± 0.8 ka ($n = 6$), 6.8 ± 0.2 ka ($n = 6$), and 7.1 ± 0.6 ka ($n = 4$), respectively.

6. Discussion

6.1. Slope stability and potential causes of sliding

Assessing the potential triggering mechanisms and causes for landsliding in our study area is challenging. This is particularly so because we have no data on the strength of rock mass discontinuities, pore water pressures, or past earthquakes for any of the four landslides. We can speculate on the triggering mechanisms, based on the mechanics of a highly idealized sliding block model, using the analysis presented in Dortch et al. (2009). The factor of safety (*FS*) against movement, which is the ratio of resisting to driving forces, for an infinite slope or rigid block resting on a planar discontinuity is easily shown from first principles to be

$$FS = (1-r)(\tan\varphi/\tan\beta) \quad (1)$$

where r is a pore- or cleft-water pressure coefficient reflecting the reduction in normal stress arising from saturation (dimensionless), φ is angle of internal friction along the potential slip surface, and β is the dip of the potential slip surface (Haneberg, 2000). Cohesion along discontinuities is ignored in this simple analysis. For non-Artesian conditions and typical rock densities, $0 \le r \le 0.4$, with the larger value reflecting complete saturation to the ground surface and slope-parallel flow. Angles of internal friction for rock mass discontinuities depend on the nature of the discontinuity and lithology, but vary generally, with $25° \le \varphi \le 45°$. As Dortch et al. (2009) showed, this basic information can be used to define three stability fields (Fig. 13). They highlight combinations of φ and β that plot within stability field 1 represent slopes that are unconditionally unstable if the dip of the discontinuities is less than the topographic slope. Slopes that plot within stability field 1 that have the discontinuities dipping more steeply than the topographic slope may fail by mechanisms such as toppling or buckling, but should not fail by frictional sliding. Combinations that plot within stability field 2 indicate slopes in which frictional elevated pore water pressures, seismic acceleration, or a combination of the two processes can trigger sliding. Long-term reduction of any cohesive strength that may exist, for example by slow movement in response to toe erosion, may also contribute to instability by reducing shear strength from peak to residual values. Slopes that plot within stability field 3 cannot be destabilized by pore water pressure alone; therefore, additional driving forces such as seismic shaking must exist for frictional block sliding to occur.

Following the approach of Dortch et al. (2009), we determined several topographic profiles of the slip surface for each landslide using SRTM DEM data and then calculated their mean dips. The slip surface of the Muztagh landslide is modified by glacial erosion, so we were unable to determine accurately the dips and it is excluded from this analysis. Comparison of the mean slip surface dips with typical angles of internal friction of the Bulunkou, Yimake, Aerpa Aigezi, Bile Jiyi, and Taheman landslides show that they plot in stability fields 1 and 2 and could therefore have been triggered by increased pore water pressure, seismic shaking, or some combination of the two (Fig. 13).

6.2. Timing of landsliding and triggers

The data that we compiled on 25 dated large landslides in the Himalaya from Dortch et al. (2009), together with the four investigated in this study, provide context for discussing the timing of sliding and triggering mechanisms in the Himalayan–Tibetan orogen (Table 3; Figs. 1 and 14). Numerical dating shows three clusters of ages: 2–3.8 ka (five landslides), 4.9–16 ka (21 landslides), and 31.8–38.9 ka (three landslides), and these correspond to periods of increased monsoon activity (Gasse et al., 1996; Shi et al., 2001). Twenty-one landslides (4.9–16 ka) occurred during the most intense monsoon phase. None of our identified landslides dates to the period ~20 ka, when monsoon activity was reduced. Taken together,

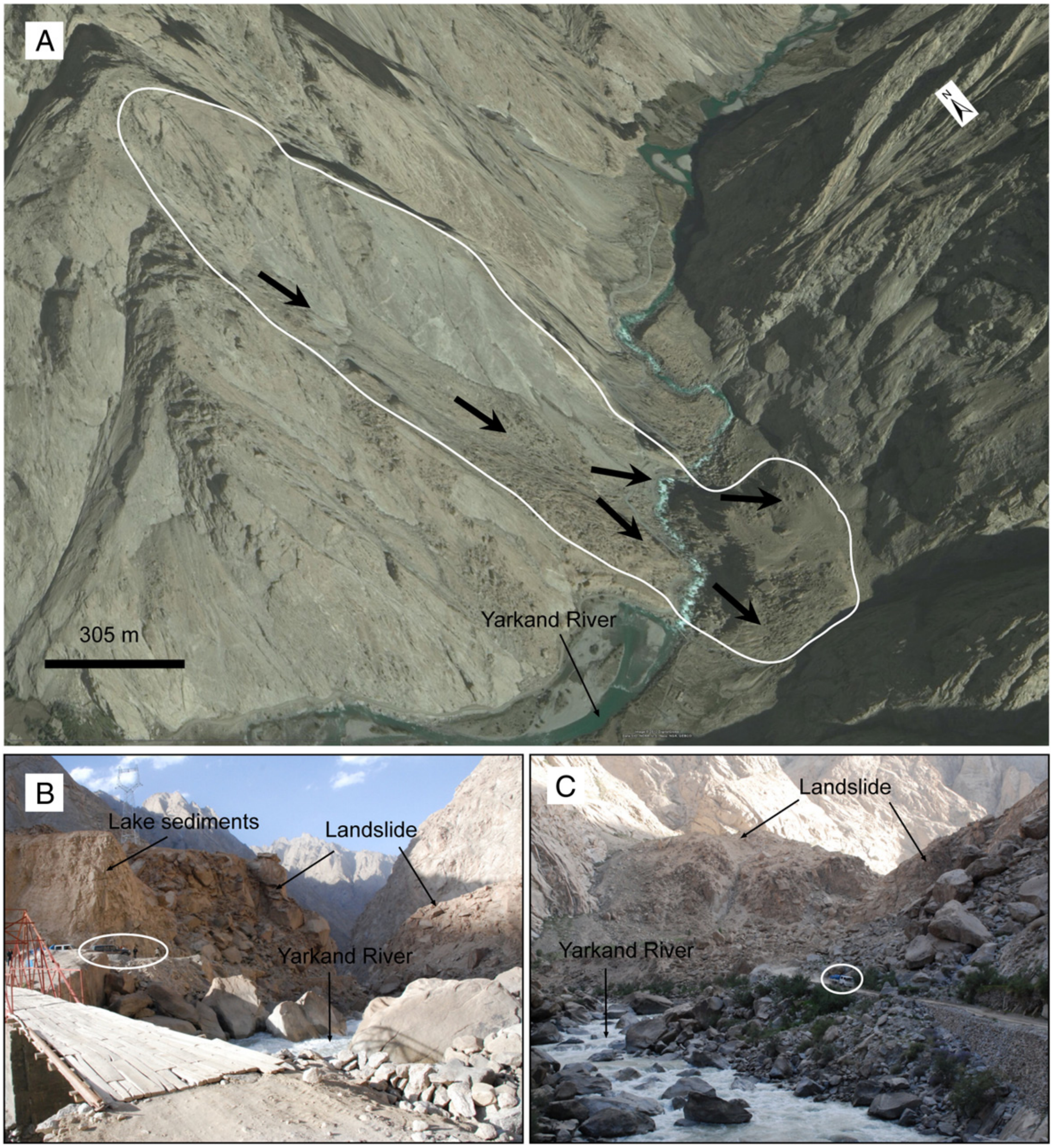

Fig. 11. Bile Jiyi landslide. (A) Google Earth image of Bile Jiyi landslide showing landslide debris accumulated on the opposite side of the valley. (B) View northeast looking downstream; and (C) view southwest looking upstream. Ellipses enclose people and vehicles for scale. Black arrows show the direction that the landslide advanced.

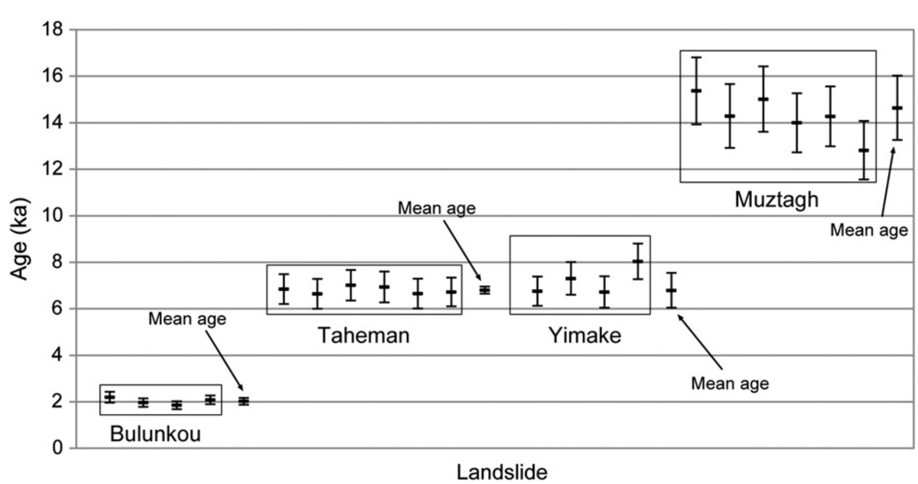

Fig. 12. ^{10}Be and arithmetic mean dates for landslides examined in this study. Arithmetic means are plotted to the right of the data block for each landslide. The data for the Taheman landslide is also presented in Yuan et al. (2012).

Table 1
Sample numbers, locations, descriptions, chemistry, and ^{10}Be dates for this study.

Sample name and landslide	Latitude °N	Longitude °E	Altitude (m asl)[a]	Boulder/clast size length/width/height (m)	Lithology	Quartz mass (g)	Be carrier (g)	Be carrier concentration (mg/g)	Be-10/Be-9 $\times 10^{-14}$	Sample thickness (cm)	Shielding correction	^{10}Be concentration (atom/g $SiO_2 \times 10^5$)	Lal (1991)/Stone (2000) Time-independent	Desilets and Zreda (2003); Desilets et al. (2006)	Dunai (2001)	Lifton et al. (2005)	Lal (1991)/Stone (2000) Time-dependent
													Age (ka)[b]	Age (ka)[b]	Age (ka)[b]	Age (ka)[b]	Age (ka)[b]
Yimake																	
Pamir-1	39.1944	75.1811	2022	<0.05	Quartz	20.8680	0.3523	1.0897	11.65 ± 0.33	2	1	1.43 ± 0.04	6.7 ± 0.6	7.6 ± 0.9	7.9 ± 1.0	7.5 ± 0.8	6.8 ± 0.6
Pamir-2	39.1974	75.1874	2013	<0.05	Quartz	20.7248	0.3517	1.0897	12.48 ± 0.41	2	1	1.54 ± 0.05	7.3 ± 0.7	8.2 ± 1.0	8.5 ± 1.1	8.1 ± 0.9	7.3 ± 0.7
Pamir-3	39.1979	75.1879	2013	<0.05	Quartz	19.1849	0.3516	1.0897	10.61 ± 0.41	2	1	1.42 ± 0.05	6.7 ± 0.7	7.6 ± 1.0	7.9 ± 1.0	7.4 ± 0.8	6.7 ± 0.7
Pamir-4	39.2002	75.1881	1997	<0.05	Quartz	20.9589	0.3519	1.0897	13.73 ± 0.43	2	1	1.68 ± 0.05	8.0 ± 0.8	9.0 ± 1.1	9.2 ± 1.2	8.8 ± 0.9	8.0 ± 0.8
Pamir-5	39.2005	75.1881	1995	<0.05	Quartz	24.9740	0.3516	1.0897	13.80 ± 0.69	2	1	1.41 ± 0.07	6.7 ± 0.8	7.7 ± 1.0	7.9 ± 1.1	7.5 ± 0.9	6.8 ± 0.7
Bulunkou																	
Pamir-44	38.7749	75.0277	3452	2.7/1.6/0.9	Gneisses	5.8990	0.3542	1.354	1.89 ± 0.09	3	0.9678	1.03 ± 0.05	2.1 ± 0.2	2.3 ± 0.3	2.5 ± 0.3	2.2 ± 0.3	2.2 ± 0.2
Pamir-45	38.7760	75.0280	3452	1.5/1.0/0.5	Gneisses	11.9314	0.3522	1.354	3.46 ± 0.08	1	0.9548	9.24 ± 0.02	1.9 ± 0.2	2.0 ± 0.2	2.3 ± 0.3	2.0 ± 0.2	2.0 ± 0.2
Pamir-46	38.7761	75.0287	3460	2.0/1.8/1.2	Gneisses	25.3648	0.3575	1.354	6.82 ± 0.19	1.5	0.9524	8.70 ± 0.02	1.8 ± 0.2	1.9 ± 0.2	2.1 ± 0.3	1.8 ± 0.2	1.9 ± 0.2
Pamir-47	38.7741	75.0276	3441	1.1/0.9/0.7	Gneisses	27.2575	0.3530	1.354	8.27 ± 0.20	3	0.9663	9.96 ± 0.02	2.0 ± 0.2	2.1 ± 0.3	2.4 ± 0.3	2.1 ± 0.2	2.1 ± 0.2
Muztagh																	
Muztagh-1	38.1470	74.9698	3658	8.0/3.1/1.6	Gneisses	29.8573	0.3507	1.414	71.42 ± 2.04	1	1	7.93 ± 0.23	15.5 ± 1.5	15.0 ± 1.9	15.3 ± 1.9	14.7 ± 1.6	15.4 ± 1.4
Muztagh-2	38.1455	74.9746	3692	5.3/4.6/3.3	Gneisses	27.6596	0.3502	1.414	62.00 ± 2.00	2	1	7.42 ± 0.24	14.3 ± 1.4	14.0 ± 1.8	14.3 ± 1.8	13.7 ± 1.5	14.3 ± 1.4
Muztagh-3	38.1461	74.9788	3746	9.0/6.5/4.0	Gneisses	28.9151	0.3515	1.414	70.01 ± 1.96	2	1	8.04 ± 0.23	15.1 ± 1.4	14.6 ± 1.8	14.9 ± 1.9	14.3 ± 1.5	15.0 ± 1.4
Muztagh-4	38.1507	74.9890	3933	6.5/4.9/3.4	Gneisses	20.3207	0.3508	1.414	50.63 ± 1.16	2	1	8.26 ± 0.19	14 ± 1.3	13.5 ± 1.7	13.8 ± 1.7	13.2 ± 1.4	14.0 ± 1.3
Muztagh-5	38.1503	74.9925	3965	4.9/4.9/3.2	Gneisses	28.6178	0.3502	1.414	74.11 ± 1.62	2	1	8.57 ± 0.19	14.3 ± 1.3	13.8 ± 1.7	14.0 ± 1.7	13.4 ± 1.4	14.3 ± 1.3
Muztagh-6	38.1424	74.9855	3780	4.7/3.2/2.8	Gneisses	18.1848	0.3489	1.414	38.72 ± 1.37	1	1	7.02 ± 0.25	12.8 ± 1.3	12.6 ± 1.6	12.9 ± 1.7	12.3 ± 1.4	12.8 ± 1.3
Muztagh-7	38.1407	74.9803	3685	4.3/3.6/3.7	Gneisses	30.7122	0.3508	1.414	70.82 ± 2.09	1	1	7.64 ± 0.23	14.7 ± 1.4	14.3 ± 1.8	14.6 ± 1.8	14.0 ± 1.5	14.6 ± 1.4
Taheman																	
P09THM-S1	38.0699	75.1831	3408	8.0/6.0/4.0	Gneisses	29.2716	0.3508	1.414	26.77 ± 0.77	2	1	3.03 ± 0.09	6.8 ± 0.7	7.2 ± 0.9	7.7 ± 1.0	7.1 ± 0.8	6.8 ± 0.6
P09THM-S2	38.0715	75.1848	3418	4.5/3.5/2.5	Gneisses	31.6510	0.3526	1.414	27.82 ± 0.91	3	1	2.93 ± 0.10	6.6 ± 0.7	7.0 ± 0.9	7.5 ± 0.9	6.9 ± 0.7	6.6 ± 0.6
P09THM-S3	38.0743	75.1855	3438	20.0/10.0/5.0	Gneisses	29.1236	0.3513	1.414	27.73 ± 0.78	2	1	3.16 ± 0.09	7.0 ± 0.7	7.4 ± 0.9	7.8 ± 1.0	7.3 ± 0.8	7.0 ± 0.7
P09THM-S4	38.0815	75.1891	3521	10.0/6.0/4.0	Gneisses	28.5264	0.3502	1.414	227.76 ± 0.84	4	1	3.22 ± 0.10	6.9 ± 0.7	7.3 ± 0.9	7.7 ± 1.0	7.1 ± 0.8	6.9 ± 0.7
P09THM-S5	38.0861	75.1910	3617	15.0/10.0/8.0	Gneisses	27.1316	0.3522	1.414	26.94 ± 0.90	2	1	3.30 ± 0.11	6.6 ± 0.7	6.9 ± 0.9	7.4 ± 0.9	6.8 ± 0.7	6.7 ± 0.6
P05C-25A	38.0919	75.1854	3751	NA	Gneisses	29.7903	0.3495	1.414	31.60 ± 0.84	5	1	3.50 ± 0.10	6.7 ± 0.6	6.9 ± 0.9	7.4 ± 0.9	6.8 ± 0.7	6.7 ± 0.6

[a] Altitudes were determined using a handheld GPS with an uncertainty of ±20 m.
[b] Ages were determined using a rock density of 2.75 g/cm^3 and 07 KNSTD standard. Uncertainties include analytical and production rate/scale model uncertainties.

Table 2
Sample numbers, locations, ^{10}Be data, and recalculated ^{10}Be dates of previously dated large landslides throughout the Himalayan–Tibetan orogeny.

Sample name and landslide	Reference source	Latitude °N	Longitude °E	Altitude (m asl)[a]	Sample thickness (cm)	Shielding correction	^{10}Be concentration (atom/g $SiO_2 \times 10^5$)	Lal (1991)/Stone (2000) Time-independent Age (ka)[b]	Desilets and Zreda (2003); Desilets et al. (2006) Age (ka)[b]	Dunai (2001) Age (ka)[b]	Lifton et al. (2005) Age (ka)[b]	Lal (1991)/Stone (2000) Time-dependent Age (ka)[b]
Darcha												
Darcha-1	Dortch et al. (2009)	32.667	77.205	3375	5	0.95	3.25 ± 0.30	9.2 ± 1.4	9.7 ± 1.7	10.1 ± 1.7	9.5 ± 1.5	9.1 ± 1.4
Darcha-2		32.668	77.205	3358	5	0.96	2.40 ± 0.14	6.8 ± 0.8	7.3 ± 1.0	7.7 ± 1.1	7.2 ± 0.9	6.7 ± 0.8
Darcha-3		32.669	77.206	3361	2	0.97	2.74 ± 0.12	7.4 ± 0.8	8.0 ± 1.1	8.4 ± 1.1	7.9 ± 0.9	7.3 ± 0.8
Darcha-4		32.669	77.205	3585	5	0.96	2.33 ± 0.21	5.8 ± 0.9	6.2 ± 1.1	6.6 ± 1.1	6.1 ± 1.0	5.8 ± 0.9
Darcha-5		32.669	77.205	3371	5	0.97	2.92 ± 0.22	8.1 ± 1.1	8.6 ± 1.4	9.1 ± 1.4	8.5 ± 1.2	8.0 ± 1.1
Darcha-6		32.669	77.206	3358	2	0.96	3.29 ± 0.61	9.0 ± 2.5	9.6 ± 2.7	10.0 ± 2.8	9.4 ± 2.6	8.9 ± 2.5
Patseo												
Patseo-2	Dortch et al. (2009)	32.755	77.257	3809	5	0.97	3.81 ± 0.23	8.3 ± 1.0	8.7 ± 1.3	9.1 ± 1.3	8.5 ± 1.1	8.2 ± 1.0
Patseo-3		32.755	77.257	3809	3	0.98	4.31 ± 0.41	9.2 ± 1.5	9.5 ± 1.7	9.9 ± 1.7	9.3 ± 1.5	9.1 ± 1.4
Patseo-4		32.754	77.258	3795	5	0.98	4.05 ± 0.47	8.8 ± 1.6	9.2 ± 1.8	9.6 ± 1.9	9.0 ± 1.7	8.7 ± 1.6
Patseo-5		32.755	77.258	3799	5	0.99	4.20 ± 0.26	9.0 ± 1.1	9.4 ± 1.4	9.8 ± 1.4	9.2 ± 1.2	8.9 ± 1.1
Patseo-6e		32.753	77.257	3801	5	0.98	5.76 ± 0.13	12.5 ± 1.2	12.6 ± 1.5	13.0 ± 1.6	12.3 ± 1.3	12.4 ± 1.1
Chilam												
Pang-1	Dortch et al. (2009)	33.962	78.211	4214	3	0.98	5.74 ± 0.19	9.8 ± 1.0	9.8 ± 1.2	10.3 ± 1.3	9.6 ± 1.1	9.7 ± 0.9
Pang-3		33.962	78.211	4213	5	0.98	5.51 ± 0.26	9.5 ± 1.0	9.6 ± 1.3	10.1 ± 1.4	9.4 ± 1.1	9.5 ± 1.0
Pang-4		33.962	78.211	4215	3	0.98	5.22 ± 0.21	8.9 ± 0.9	9.0 ± 1.2	9.5 ± 1.2	8.8 ± 1.0	8.8 ± 0.9
Pang-5		33.962	78.211	4217	5	0.98	5.83 ± 0.32	10.1 ± 1.2	10.1 ± 1.4	10.5 ± 1.5	9.9 ± 1.2	10.0 ± 1.2
Pang-6		33.962	78.211	4216	5	0.98	5.79 ± 0.20	10 ± 1.0	10.0 ± 1.3	10.5 ± 1.3	9.8 ± 1.1	10.0 ± 1.0
Pang-7		33.962	78.212	4212	4	0.98	5.56 ± 0.17	9.6 ± 0.9	9.6 ± 1.2	10.1 ± 1.3	9.4 ± 1.0	9.5 ± 0.9
Kelang Serai												
COS1	Dortch et al. (2009); Mitchell et al. (2007)	32.816	77.441	5000	2	0.99	5.87 ± 0.23	6.9 ± 0.7	6.8 ± 0.9	7.3 ± 0.9	6.7 ± 0.8	6.8 ± 0.7
COS2		32.816	77.448	4717	2	0.99	5.12 ± 0.23	6.8 ± 0.7	6.9 ± 0.9	7.3 ± 1.0	6.8 ± 0.8	6.8 ± 0.7
COS3		32.822	77.459	4780	2	0.99	5.24 ± 0.23	6.8 ± 0.7	6.8 ± 0.9	7.3 ± 1.0	6.7 ± 0.8	6.7 ± 0.7
India-2		32.82	77.455	4621	2	1	5.13 ± 0.25	7.1 ± 0.8	7.2 ± 1.0	7.6 ± 1.0	7.1 ± 0.9	7.0 ± 0.8
India-3		32.821	77.455	4621	3	1	5.11 ± 0.32	7.1 ± 0.9	7.2 ± 1.1	7.7 ± 1.1	7.1 ± 0.9	7.0 ± 0.9
India-4		32.821	77.455	4625	3	1	4.90 ± 0.19	6.8 ± 0.7	6.9 ± 0.9	7.4 ± 0.9	6.8 ± 0.8	6.7 ± 0.7
India-5		32.82	77.454	4638	4	0.98	5.38 ± 0.25	7.6 ± 0.8	7.7 ± 1.0	8.1 ± 1.1	7.6 ± 0.9	7.5 ± 0.8
India-6		32.82	77.454	4635	2	0.98	5.71 ± 0.29	8.0 ± 0.9	8.0 ± 1.1	8.4 ± 1.2	7.9 ± 1.0	7.9 ± 0.9
India-7		32.82	77.454	4634	4	1	5.69 ± 0.32	7.9 ± 0.9	8.0 ± 1.1	8.4 ± 1.2	7.8 ± 1.0	7.8 ± 0.9
India-8		32.818	77.451	4682	4	1	5.24 ± 0.20	7.1 ± 0.7	7.2 ± 0.9	7.7 ± 1.0	7.1 ± 0.8	7.1 ± 0.7
India-9		32.82	77.447	4650	2	0.98	5.43 ± 0.24	7.5 ± 0.8	7.6 ± 1.0	8.0 ± 1.1	7.5 ± 0.9	7.4 ± 0.8
Tianchi												
TCB-1	Yi et al. (2006)	43.902	88.122	1923	2	0.98	2.52 ± 0.25	12.8 ± 2.1	13.4 ± 2.4	13.6 ± 2.4	13.1 ± 2.2	12.9 ± 2.1
TCB-2		43.901	88.121	1944	2	0.98	4.10 ± 0.14	20.5 ± 2.0	20.9 ± 2.7	21.0 ± 2.7	20.4 ± 2.3	20.4 ± 2.0
TCB-3		43.9	88.121	1938	2	0.98	3.02 ± 0.40	15.2 ± 3.1	15.7 ± 3.4	15.9 ± 3.5	15.4 ± 3.3	15.2 ± 3.1
TCB-6		43.897	88.118	1944	2	0.98	2.53 ± 0.14	12.6 ± 1.5	13.2 ± 1.9	13.4 ± 1.9	13.0 ± 1.6	12.7 ± 1.5
TCB-7		43.898	88.119	1922	2	0.98	1.66 ± 0.15	8.4 ± 1.3	9.0 ± 1.5	9.2 ± 1.6	8.8 ± 1.4	8.5 ± 1.3
Rangatoli												
G1	Barnard et al. (2001)	30.389	79.334	1330	2	1	3.72 ± 0.04	3.7 ± 0.6	4.6 ± 0.8	4.6 ± 0.8	4.6 ± 0.8	3.8 ± 0.7
G2		30.389	79.334	1335	2	0.99	3.05 ± 0.03	3.0 ± 0.5	3.8 ± 0.7	3.8 ± 0.7	3.8 ± 0.6	3.2 ± 0.5
G3		30.389	79.333	1340	2	0.99	7.97 ± 0.06	7.9 ± 1.1	9.3 ± 1.4	9.4 ± 1.4	9.2 ± 1.3	7.8 ± 1.1
Dear												
G4	Barnard et al. (2001)	30.422	79.347	1490	2	1	1.22 ± 0.04	10.9 ± 1.1	12.4 ± 1.6	12.4 ± 1.6	12.1 ± 1.3	10.7 ± 1.0
G5		30.422	79.347	1490	2	0.99	1.30 ± 0.05	11.7 ± 1.2	13.3 ± 1.7	13.3 ± 1.7	13.0 ± 1.4	11.6 ± 1.2
G6		30.422	79.348	1485	2	1	1.23 ± 0.04	11 ± 1.1	12.6 ± 1.6	12.6 ± 1.6	12.2 ± 1.3	10.9 ± 1.0
G7		30.429	79.348	1530	2	0.99	1.21 ± 0.05	10.6 ± 1.1	12.1 ± 1.6	12.1 ± 1.6	11.8 ± 1.3	10.5 ± 1.1
G8		30.429	79.349	1530	2	0.99	1.20 ± 0.05	10.5 ± 1.1	12.0 ± 1.6	12 ± 1.6	11.7 ± 1.3	10.4 ± 1.1
Milan												
NDL24	Barnard et al. (2004)	30.43	80.16	3446	2	0.97	1.90 ± 0.65	5.3 ± 2.6	5.7 ± 2.7	5.9 ± 2.8	5.7 ± 2.7	5.3 ± 2.6
NDL25		30.43	80.16	3335	2	0.97	3.14 ± 0.14	9.3 ± 1.0	9.8 ± 1.3	10.2 ± 1.3	9.6 ± 1.1	9.1 ± 1.0
NDL26		30.43	80.16	3416	2	0.97	2.82 ± 0.16	8.0 ± 0.9	8.4 ± 1.2	8.9 ± 1.2	8.3 ± 1.1	7.8 ± 0.9
NDL27		30.43	80.16	3435	2	0.97	3.23 ± 0.80	9.0 ± 3.3	9.5 ± 3.4	9.9 ± 3.5	9.3 ± 3.4	8.9 ± 3.2
Yaral												
E99	Barnard et al. (2006)	27.85	86.8	4114	2	0.98	4.34 ± 0.11	8.9 ± 0.8	8.9 ± 1.1	9.5 ± 1.2	8.8 ± 0.9	8.8 ± 0.8
E100		27.85	86.8	4058	2	0.98	4.14 ± 0.11	8.8 ± 0.8	8.8 ± 1.1	9.4 ± 1.2	8.7 ± 0.9	8.6 ± 0.8
E101		27.85	86.8	4058	2	0.98	4.23 ± 0.13	9.0 ± 0.9	9.0 ± 1.1	9.6 ± 1.2	8.8 ± 1.0	8.8 ± 0.8

Table 2 (*continued*)

Sample name and landslide	Reference source	Latitude °N	Longitude °E	Altitude (m asl)[a]	Sample thickness (cm)	Shielding correction	^{10}Be concentration (atom/g $SiO_2 \times 10^5$)	Lal (1991)/Stone (2000) Time-independent	Desilets and Zreda (2003); Desilets et al. (2006)	Dunai (2001)	Lifton et al. (2005)	Lal (1991)/Stone (2000) Time-dependent
								Age (ka)[b]	Age (ka)[b]	Age (ka)[b]	Age (ka)[b]	Age (ka)[b]
Pangbache												
E109	Barnard et al. (2006)	27.86	86.79	3985	2	0.98	4.96 ± 0.23	10.9 ± 1.2	10.9 ± 1.5	11.4 ± 1.5	10.6 ± 1.3	10.8 ± 1.2
E110		27.85	86.79	3970	2	0.98	11.2 ± 0.34	24.9 ± 2.4	22.8 ± 2.9	23.2 ± 2.9	21.9 ± 2.4	23.3 ± 2.2
E111		27.85	86.79	3979	2	0.98	4.29 ± 0.13	9.5 ± 09	9.5 ± 1.2	10.1 ± 1.3	9.4 ± 1.0	9.3 ± 0.9
Tsergo Ri												
KTM10	Barnard et al. (2006)	28.209	85.608	4831	2	0.99	33.7 ± 0.83	49.4 ± 4.7	38.3 ± 4.8	37.9 ± 4.7	36.6 ± 3.9	41.5 ± 3.9
KTM11		28.209	85.608	4843	2	0.99	18.0 ± 0.37	26.1 ± 2.4	22.8 ± 2.8	23.1 ± 2.8	21.7 ± 2.3	24.3 ± 2.2
KTM12		28.209	85.608	4848	2	0.99	28.5 ± 0.44	41.4 ± 3.7	33.5 ± 4.1	33.3 ± 4.0	31.8 ± 3.3	36.2 ± 3.2
Gomboro												
K2-36	Shroder et al. (2011)	35.729	75.663	2828	2	0.94	4.65 ± 0.13	16.6 ± 1.6	17.0 ± 2.1	17.2 ± 2.1	16.6 ± 1.8	16.4 ± 1.5
K2-37		35.729	75.663	2833	2	0.95	4.76 ± 0.13	16.8 ± 1.6	17.2 ± 2.1	17.3 ± 2.1	16.8 ± 1.8	16.5 ± 1.5
K2-38		35.73	75.663	2832	2	0.95	4.82 ± 0.15	17 ± 1.7	17.4 ± 2.2	17.5 ± 2.2	17 ± 1.8	16.7 ± 1.6
K2-39		35.73	75.662	2837	2	0.95	4.60 ± 0.13	16.2 ± 1.6	16.6 ± 2.1	16.8 ± 2.1	16.2 ± 1.7	16.0 ± 1.5
K2-40		35.73	75.662	2835	2	0.95	4.61 ± 0.13	16.2 ± 1.6	16.7 ± 2.1	16.8 ± 2.1	16.3 ± 1.7	16.0 ± 1.5
K2-41		35.729	75.663	2839	2	0.95	4.04 ± 0.16	14.2 ± 1.5	14.8 ± 1.9	15.0 ± 2.0	14.5 ± 1.6	14.1 ± 1.4
Rongbuk												
Ron 68	Owen et al. (2008)	28.2023	86.8235	5028	1.5	0.99	7.12 ± 0.21	9.4 ± 0.9	9.0 ± 1.1	9.6 ± 1.2	8.8 ± 1.0	9.3 ± 0.9
Ron 69		28.2024	86.8236	5013	1	0.99	7.29 ± 0.19	9.7 ± 0.9	9.3 ± 1.1	9.8 ± 1.2	9.0 ± 1.0	9.6 ± 0.9
Ron 70		28.2024	86.8235	5009	3	0.99	6.67 ± 0.17	9.0 ± 0.9	8.6 ± 1.1	9.2 ± 1.1	8.5 ± 0.9	8.9 ± 0.8
Ron 71		28.2019	86.8235	5015	2.5	0.97	7.00 ± 0.14	9.6 ± 0.9	9.2 ± 1.1	9.7 ± 1.2	9.0 ± 0.9	9.5 ± 0.8
Ron 72		28.2018	86.8243	5031	4	0.98	6.93 ± 0.17	9.5 ± 0.9	9.0 ± 1.1	9.6 ± 1.2	8.8 ± 0.9	9.3 ± 0.9
Ron 73A		28.2015	86.8246	5019	3	0.98	6.74 ± 0.18	9.2 ± 0.9	8.8 ± 1.1	9.3 ± 1.2	8.6 ± 0.9	9.0 ± 0.8
Ron 73B		28.2015	86.8246	5019	3	0.98	7.00 ± 0.18	9.5 ± 0.9	9.1 ± 1.1	9.7 ± 1.2	8.9 ± 0.9	9.4 ± 0.9
Katzarah												
KATZ II	Hewitt et al. (2011)	35.428	75.46	2310	5	0.972	1.56 ± 0.03	6.9 ± 0.6	7.9 ± 1.0	8.2 ± 1.0	7.8 ± 0.8	6.9 ± 0.6
KATZ IV		35.443	75.4333	2500	6	0.96	1.67 ± 0.04	6.7 ± 0.6	7.6 ± 0.9	7.9 ± 1.0	7.5 ± 0.8	6.7 ± 0.6
Gol Ghone												
GG I	Hewitt et al. (2011)	35.285	75.8667	2590	8	1	0.94 ± 0.04	3.5 ± 0.4	4.1 ± 0.5	4.4 ± 0.6	4.0 ± 0.5	3.7 ± 0.4
GG II		35.285	75.8667	2590	8	1	0.89 ± 0.03	3.3 ± 0.3	3.8 ± 0.5	4.1 ± 0.5	3.8 ± 0.4	3.5 ± 0.3
Satpara-Skardu												
STSK I	Hewitt et al. (2011)	35.248	75.6283	2850	8	1	1.09 ± 0.03	3.5 ± 0.3	4.0 ± 0.5	4.3 ± 0.5	3.9 ± 0.4	3.6 ± 0.3
STSK II		35.247	75.6283	2850	2	0.97	1.15 ± 0.03	3.6 ± 0.3	4.1 ± 0.5	4.4 ± 0.5	4.1 ± 0.4	3.7 ± 0.3
STSK III		35.233	75.6283	2850	8	1	1.06 ± 0.03	3.4 ± 0.3	3.9 ± 0.5	4.2 ± 0.5	3.8 ± 0.4	3.5 ± 0.3
Dhak Chauki												
DCh II	Hewitt et al. (2011)	35.895	74.435	1500	8	1	0.73 ± 0.02	5.5 ± 0.5	6.6 ± 0.8	6.8 ± 0.8	6.5 ± 0.7	5.6 ± 0.5
DCh III		35.895	74.435	1500	8	1	0.71 ± 0.02	5.4 ± 0.5	6.4 ± 0.8	6.5 ± 0.8	6.3 ± 0.7	5.5 ± 0.5
Upper Henzul												
Uhen I	Hewitt et al. (2011)	35.996	74.2	1800	0.7	0.982	1.25 ± 0.03	7.4 ± 0.7	8.5 ± 1.0	8.7 ± 1.1	8.4 ± 0.9	7.3 ± 0.7
Uhen II		35.996	74.2	1810	1.5	0.982	2.36 ± 0.06	13.9 ± 1.3	15.3 ± 1.9	15.3 ± 1.9	15 ± 1.6	13.9 ± 1.3
Uhen III		35.996	74.2	1800	8	1	1.15 ± 0.03	7.0 ± 0.7	8.2 ± 1.0	8.4 ± 1.0	8.1 ± 0.8	7.0 ± 0.6
Baltit-Sumayar												
BaSu I	Hewitt et al. (2011)	36.304	74.673	2200	3	0.967	0.83 ± 0.02	3.8 ± 0.4	4.5 ± 0.5	4.7 ± 0.6	4.5 ± 0.5	4.0 ± 0.4
BaSu II		36.304	74.673	2200	2	0.967	0.80 ± 0.02	3.7 ± 0.3	4.3 ± 0.5	4.5 ± 0.6	4.2 ± 0.4	3.8 ± 0.4
BaSu III		36.304	74.6738	2195	3	0.967	0.75 ± 0.02	3.5 ± 0.3	4.1 ± 0.5	4.3 ± 0.5	4.0 ± 0.4	3.6 ± 0.3

[a] Altitudes were determined using a handheld GPS with an uncertainty of ±20 m.
[b] Ages were determined using a rock density of 2.75 g/cm^3 and 07 KNSTD standard. Uncertainties include analytical and production rate/scale model uncertainties.

this evidence suggests that landsliding intensity is directly proportional to the intensity of monsoon.

Geologic factors may also greatly influence landsliding in this region. The proximity of the landslides to the active Kongur extensional system (Robinson et al., 2004, 2007) strongly suggests a link between seismic shaking and landslide initiation. Geologic structure also likely plays an important role. The Kongur Shan and Muztagh Ata gneiss domes in the footwall of the Kongur extensional system have experienced rapid exhumation since ~7 Ma (Robinson et al., 2010). Footwall exhumation has led to steeply dipping foliations and the formation of triangular facets along the range. Glaciation and periglacial weathering also steepen and fracture slopes. Landslides could easily occur in this kind of setting, as is likely the case for the Bulunkou, Muztagh, and Taheman landslides. As for the Yimake landslide, the bedrock is foliated, cut by several sets of joints, and heavily fractured (Fig. 9D and E). These fractures likely weakened the rockslope and enabled the generally planar scar to form (Dortch et al., 2009). Thus geology, seismic shaking, and increased monsoon precipitation could all be factors in controlling the location and timing of landsliding in the Pamir.

Table 3
Summary of large landslides ages (using the Lal(1991)/Stone(2000) time-dependent scaling model) for those numerically dated in the Himalayan–Tibetan orogen organized from youngest to oldest.

Landslide	Latitude	Longitude	Volume ($\times 10^6$ m^3)	Type	Average age[a] (ka)	Author
Bulunkou	38.775	75.028	17	^{10}Be	2.0 ± 0.1	This study
Kaza	32.18	78.09	500	^{14}C	3.0 ± 0.1	Bookhagen et al. (2005)
Gol Ghone	35.285	75.8667	1.4	^{10}Be	3.6 ± 0.1	Hewitt et al. (2011)
Satpara-Skardu	35.248	75.6283	1.4	^{10}Be	3.6 ± 0.1	Hewitt et al. (2011)
Baltit-Sumayar	36.304	74.673	1	^{10}Be	3.8 ± 0.2	Hewitt et al. (2011)
Rangatoli	30.389	79.334	N/A	^{10}Be	4.9 ± 2.5	Barnard et al. (2001)
Dhak Chauki	35.895	74.435	1.1	^{10}Be	5.5 ± 0.1	Hewitt et al. (2011)
Kuppa	31.43	78.24	600	^{14}C	6.1 ± 8.4[d]	Bookhagen et al. (2005)
Taheman	38.0743	75.1855	155	^{10}Be	6.8 ± 0.2	This study
Katzarah	35.443	75.4333	2.1	^{10}Be	6.8 ± 0.1	Hewitt et al. (2011)
Yimake	39.1979	75.1879	1400	^{10}Be	7.1 ± 0.6	This study
Upper Henzul	35.996	74.2	0.8	^{10}Be	7.2 ± 0.2[b]	Hewitt et al. (2011)
Kelang Serai	32.816	77.441	520–900	^{10}Be	7.2 ± 0.4	Mitchell et al. (2007) Dortch et al. (2009)
Darcha	32.667	77.205	10	^{10}Be	7.6 ± 1.3	Dortch et al. (2009)
Sichling	32.11	78.18	1400	^{14}C	7.6 ± 0.1–9.7 ± 0.1[d]	Bookhagen et al. (2005)
Milan	30.43	80.16	N/A	^{10}Be	7.8 ± 1.7[c]	Barnard et al. (2004)
Ghoro Choh	35.64	75.5	60	^{14}C	<7.95[d]	Hewitt (1999)
Yaral	27.85	86.8	N/A	^{10}Be	8.7 ± 0.1[c]	Barnard et al. (2006)
Patseo	32.76	77.26	128	^{10}Be	8.7 ± 0.4[e]	Dortch et al. (2009)
Rongbuk	28.2023	86.8235	2	^{10}Be	9.3 ± 0.2	Owen et al. (2008)
Chilam	33.962	78.211	240	^{10}Be	9.6 ± 0.4	Dortch et al. (2009)
Pangbache	27.86	86.79	N/A	^{10}Be	10.1 ± 1.0[c,f]	Barnard et al. (2006)
Dear	30.422	79.347	N/A	^{10}Be	10.8 ± 0.5	Barnard et al. (2001)
Tianchi	43.902	88.122	N/A	^{10}Be	13.6 ± 1.4[g]	Yi et al. (2006)
Muztagh	38.147	74.9698	480	^{10}Be	14.3 ± 0.8	This study
Gomboro	35.729	75.663	N/A	^{10}Be	16.0 ± 1.0	Shroder et al. (2011)
Shaso	31.72	78.51	600	^{14}C	<31.8 ± 0.5[d]	Bookhagen et al. (2005)
Chango	32.07	78.59	1000	^{14}C	<33.1 ± 0.3[d]	Bookhagen et al. (2005)
Tsergo Ri	28.209	85.608	10,000	^{10}Be	38.9 ± 3.8[h]	Barnard et al. (2006)

[a] Uncertainty expressed as 1 σ.
[b] Sample Uhen II not included in calculation as 3 σ beyond average.
[c] Landslides Dortch et al. (2009) missed.
[d] Calibrated using CalPal (Dortch et al., 2009).
[e] Samples Patseo-6 not included in calculation as 3σ beyond average.
[f] Sample E110 not included in calculation as 3 σ beyond average.
[g] Sample TCB-2 and TCB-7 not included in calculation as 3 σ beyond average.
[h] Sample KTM 11 not included in calculation as 3 σ beyond average.

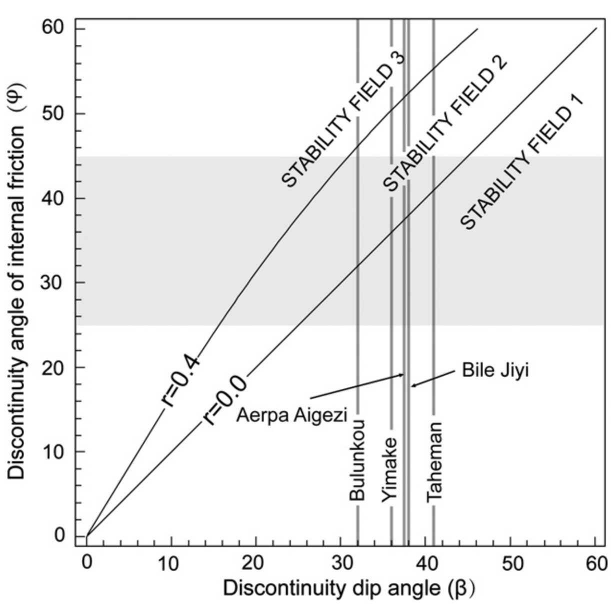

Fig. 13. Large landslides examined in this study plotted on idealized stability fields for frictional block sliding based on discontinuity dip and angle of internal friction (modified from Dortch et al., 2009). Stability field 1 is unconditionally unstable; stability field 2 can be destabilized by an increase in pore-water pressure during seismic shaking; and stability field 3 requires seismic shaking for destabilization. Gray horizontal shading indicates typical angles of internal friction.

6.3. Importance of large landslides in landscape development

Large landslides are clearly important in helping to shape high mountains, as exhibited by the numerous landslide scars and debris piles that are present throughout the world's orogenic belts (e.g., Hewitt, 1988, 1998, 2009; Shroder and Bishop, 1998; Korup et al., 2007; Hewitt et al., 2008, 2011; Seong et al., 2008, 2009a; Hancox and Perrin, 2009; Shulmeister et al., 2009; Parker et al., 2011). Various studies have linked fluvial and glacial processes, particularly during times of climatic instability, to landsliding (Ballantyne and Benn, 1994; Ballantyne, 2002, 2004; Barnard et al., 2004; Borgatti and Soldati, 2010a,b; Fort et al., 2010), many of which are large (>1 million m^3). Some studies emphasize that threshold slopes exist where continuous slope failure is associated with rapid uplift (e.g., Burbank et al., 1996) and that areas of rapid uplift are often prone to large landsliding. In particular, Shroder et al. (2011) discussed the concept of a denudation cascade within an active orogen, the Karakoram, that begins with weathering and mass movement processes, such as snow and ice avalanches, slow sackungen, rock falls and rockslides, rapid wet debris flows, and profuse talus and colluvial accumulations.

Despite the plethora of studies emphasizing the important links between landsliding and landscape development, few studies have quantified the relative role of large mass movement to overall landscape development in high mountains, particularly in the Himalayan–Tibetan orogen. This is partially because of the lack of regional mapping, but also because of difficulties in dating ancient landslides.

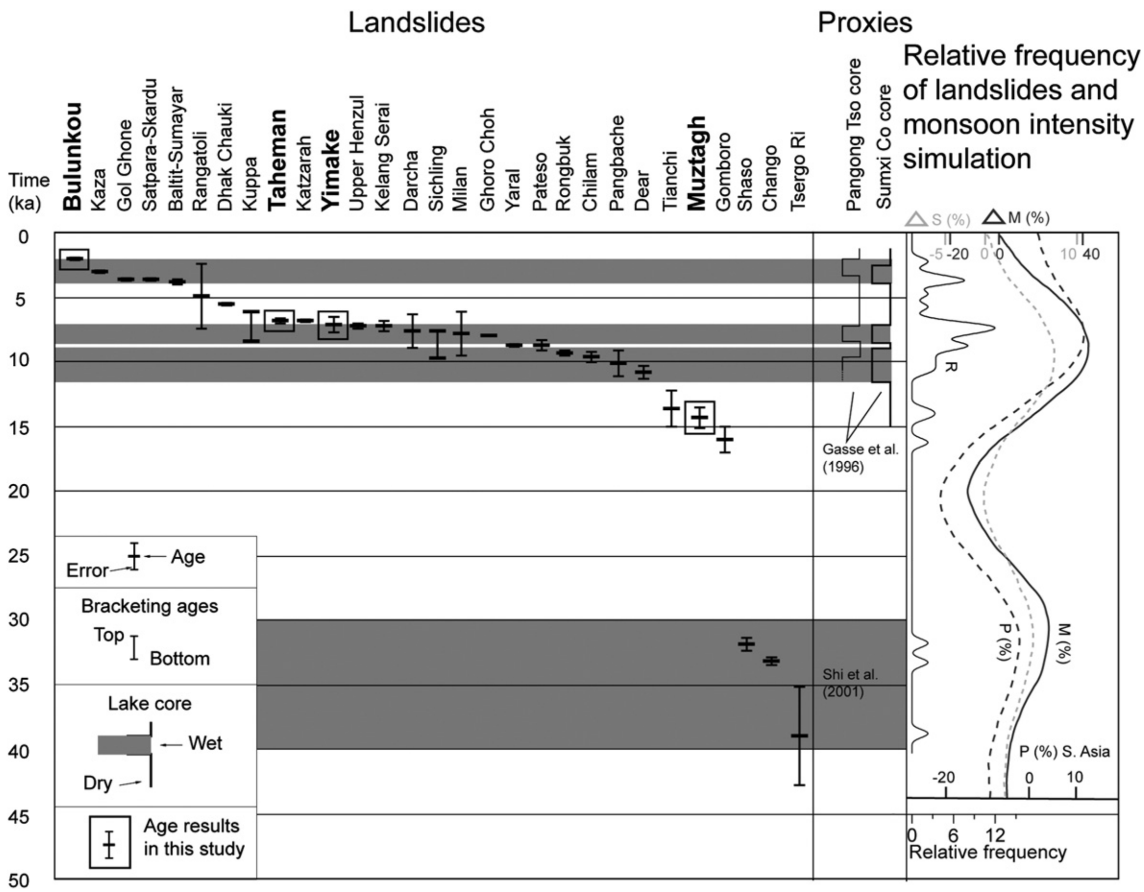

Fig. 14. Plots of large landslides ages in Table 2 for those numerically dated in the Himalayan–Tibetan orogen and curves of monsoon intensity and precipitation based on lake cores (modified from Dortch et al., 2009; plus data from Hewitt et al., 2011; Shroder et al., 2011; and Yuan et al., 2012). The relative frequency (*R* relative frequency, thin black line) for all the landslides ages is plotted next to the monsoon/precipitation curves.

Korup and Clague (2009) point out that known landslides in the Himalayas affect <1% of the orogen's total area, as opposed to 10% in the Alps, the latter having much less relief and being tectonically less active. Hewitt et al. (2008) and Korup and Clague (2009) attributed this difference to significant undersampling of such events and suggested the role of landsliding in the Himalaya is probably much greater than currently believed. Moreover, quantifying the importance of different triggering mechanisms is challenging, especially for landslides older than a few decades/centuries in regions where little or no historical is documented. This is particularly so in the Himalayan–Tibetan orogen where few historical documents and/or accounts exist.

In our extensive study using Google Earth, we recognized four new giant landslides >1 million m^3 in size in an area of ~27,700 km^2. We acknowledge the possibility that we have not identified other large landslides in the region because they have been eroded away or because the available imagery was not good enough for such regional mapping. Since the data on large landslides in the Himalayan–Tibetan orogen is sparse, it is not possible to say at this time whether the frequency of large landslides in our study area is typical of the orogen as a whole. However, our new data provide an important step, together with the studies cited by Dortch et al. (2009), toward understanding the magnitude and frequency of large landslides in the Himalayan–Tibetan orogen.

Using the data for our large landslides, we are able to estimate the amount of debris involved in large landsliding since ~14 ka (the age of our oldest dated landslide). Debris volumes were calculated as the product of the debris planimetric areas and typical thickness values visually estimated from Google Earth, SRTM DEMs, or measured using a TruPulse 200 Rangefinder. The thickness estimates are subjective and do not account for any topography buried beneath the landslide debris; their accuracy is probably no better than 25%. The total volume of debris moved by large landslides since the Late Glacial is ~2168 million m^3. This equates to ~78 mm (2168 million m^3/ 27,700 km^2) of surface lowering of the landscape by large landslides since the Late Glacial, or the equivalent to a lowering of the landscape of 0.005 mm a^{-1} over that time (presuming all landslide debris will be eventually transported from the region). This is an order of magnitude greater than that determined by Barnard et al. (2001) in the Garhwal Himalaya where they calculated a net landscape lowering of 0.0004 mm a^{-1} because of large Holocene landslides. Our estimate also contrasts with other studies such as that of Dortch et al. (2009) who show that the average landscape lowering in Lahul owing to large landslides during the Holocene was ~0.12 mm a^{-1} and such as Korup et al.'s (2007) estimate of ≤0.01 mm a^{-1} in areas of high uplift (>4 mm a^{-1}). These differences illustrate the need to undertake extensive quantitative studies of large landslides to fully assess their relative roles in the development of high mountain landscapes. Clearly, the role of smaller landslides and other processes also needs to be fully quantified to understand the greater significance of large landslides in landscape development in these regions.

7. Conclusion

Increased pore water pressure, seismic shaking, or some combination of the two likely triggered the large landslides that we examined in this study. Our dating of the Bulunkou, Muztagh, Taheman, and Yimake landslides showed that they occurred in times of increased precipitation. The timing of many other large landslides in the Himalayan–Tibetan orogen at ~2–3.8 ka, ~4.9–16 ka, and ~32–39 ka also suggests that during periods of increased precipitation large landsliding is prevalent. We argue that climatic strongly controls the development of large landslides in the Himalayan–Tibetan orogen while still acknowledging the importance of earthquakes as a mechanism to help initiate landslides in these tectonically active regions. Extensive regional mapping, detailed analysis of landforms, and dating of large and small landslides in the Himalayan–Tibetan orogen is needed to fully access the causal factors for landsliding and the role of landsliding in landscape development. Our study provides a first step toward this goal in the northwestern portion of the orogen.

Acknowledgments

This research was supported by grants from the State Key Laboratory of Earthquake Dynamics of China (no. LED2010A04), the National Science Foundation of China (41272195), the National Science Foundation of the U.S. (EAR-0910759), the International Science and Technology Cooperation Program of China (2008DFA20860). We thank three anonymous reviewers for their very constructive and useful comments that helped improve our manuscript and Professor Richard Marston for his positive and extremely detailed editing of our manuscript.

References

Arnaud, N.O., Bruel, M., Cantagrel, J.M., Tapponnier, P., 1993. High cooling and denudation rates at Kongur Shan, eastern Pamir (Xinjiang, China) revealed by $^{40}Ar/^{39}Ar$ alkali feldspar thermochronology. Tectonics 12, 1335–1346.

Balco, G., Stone, J.O., Lifton, N.A., Dunai, T.J., 2008. A complete and easily accessible means of calculating surface exposure ages or erosion rates from ^{10}Be and ^{26}Al measurements. Quaternary Geochronology 3, 174–195.

Ballantyne, C.K., 2002. Paraglacial geomorphology. Quaternary Science Reviews 21, 1935–2017.

Ballantyne, C.K., 2004. Paraglacial landsystems. In: Evans, D.J. (Ed.), Glacial Landsystems. Edward Arnold, London, pp. 432–461.

Ballantyne, C.K., Benn, D.I., 1994. Paraglacial slope adjustment and resedimentation following recent glacier retreat, Fabergstolsdalen, Norway. Arctic and Alpine Research 26, 255–269.

Barnard, P.l, Owen, L.A., Sharma, M.C., Finkel, R.C., 2001. Natural and human-induced landsliding in the Garhwal Himalaya of northern India. Geomorphology 40, 21–35.

Barnard, P.L., Owen, L.A., Sharma, M.C., Finkel, R.C., 2004. Late Quaternary (Holocene) landscape evolution of a monsoon-influenced high Himalayan valley, Gori Ganga, Nanda Devi, NE Garhwal. Geomorphology 61, 91–110.

Barnard, P.l, Owen, L.A., Finkel, R.C., 2006. Quaternary fans and terraces in the Khumbu Himal south of Mount Everest: their characteristics, age and formation. Journal of the Geological Society of London 163, 383–399.

Bookhagen, B., Thiede, R.C., Strecker, M.R., 2005. Late Quaternary intensified monsoon phases control landscape evolution in the northwest Himalaya. Geology 33, 149–152.

Borgatti, L., Soldati, M., 2010a. Landslides as a geomorphological proxy for climate change: a record from the Dolomites (northern Italy). Geomorphology 120, 56–64.

Borgatti, L., Soldati, M., 2010b. Landslides and climatic change. In: Alcantara Ayala, I., Goudie, A. (Eds.), Geomorphological Hazards and Disaster Prevention. Cambridge University Press, pp. 87–95.

Brunel, M., Arnaud, N., Tapponnier, P., Pan, Y., Wang, Y., 1994. Kongur Shan normal fault: type example of mountain building assisted by extension (Karakoram fault, eastern Pamir). Geology 22, 707–710.

Burbank, D.W., Leland, J., Fielding, E., Anderson, R.S., Brozovic, N., Reed, M.R., Duncan, C., 1996. Bedrock incision, rock uplift and threshold hillslopes in the northwestern Himalayas. Nature 379, 505–510.

Burtman, V.S., Molnar, P., 1993. Geological and Geophysical Evidence for Deep Subduction of Continental Crust Beneath the Pamir. Special Paper 281. Geological Society of America, Boulder, Colorado, pp. 1–76.

Desilets, D., Zreda, M., 2003. Spatial and temporal distribution of secondary cosmic-ray nucleon intensities and applications to in situ cosmogenic dating. Earth and Planetary Science Letters 206, 21–42.

Desilets, D., Zreda, M., Prabu, T., 2006. Elevation dependence of cosmogenic ^{36}Cl production in Hawaiian lava flows. Earth and Planetary Science Letters 246, 277–287.

Dortch, J., Owen, L.A., Haneberg, W.C., Caffee, M.W., Dietsch, C., Kamp, U., 2009. Nature and timing of mega-landslides in northern India. Quaternary Science Reviews 28, 1037–1054.

Dunai, T.J., 2001. Influence of secular variation of the magnetic field on production rates of in situ produced cosmogenic nuclides. Earth and Planetary Science Letters 193, 197–212.

Fort, M., Peulvast, J., 1995. Catastrophic mass-movements and morphogenesis in the Peri-Tibetan Ranges: examples for west Kunlun, east Pamir and Ladakh. In: Slaymaker, O. (Ed.), Steepland Geomorphology. Wiley, New York, pp. 171–198.

Fort, M., Cossart, E., Arnaud-Fassetta, G., 2010. Hillslope–channel coupling in the Nepal Himalayas and threat to man-made structures: the middle Kali Gandaki Valley. Geomorphology 124, 178–199.

Gasse, F., Fontes, J.C., Van Campo, E., Wei, K., 1996. Holocene environmental changes in Bangong Co basin (western Tibet). Part 4: discussion and conclusions. Paleogeography, Paleoclimatology, Paleoecology 120, 79–92.

Hancox, G.T., Perrin, N.J., 2009. Green Lake landslide and other giant and very large postglacial landslides in Fiordland, New Zealand. Quaternary Science Reviews 28, 1020–1036.

Haneberg, W.C., 2000. Deterministic and probabilistic approaches to geologic hazard assessment. Environmental and Engineering Geoscience 6, 209–226.

Hewitt, K., 1988. Catastrophic landslide deposits in the Karakoram Himalaya. Science 242, 64–67.

Hewitt, K., 1998. Catastrophic landslides and their effects on the Upper Indus streams, Karakoram Himalaya, northern Pakistan. Geomorphology 26, 47–80.

Hewitt, K., 1999. Quaternary moraines vs catastrophic rock avalanches in the Karakoram Himalaya, northern Pakistan. Quaternary Research 51, 220–237.

Hewitt, K., 2009. Catastrophic rock slope failures and late Quaternary developments in the Nanga Parbat–Haramosh massif, Upper Indus basin, northern Pakistan. Quaternary Science Reviews 28, 1085–1096.

Hewitt, K., Clague, J.J., Orwin, J.F., 2008. Legacies of catastrophic rock slope failures in mountain landscapes. Earth-Science Reviews 87, 1–38.

Hewitt, K., Gosse, J., Clague, J.J., 2011. Rock avalanches and the pace of late Quaternary development of river valleys in the Karakoram Himalaya. Geological Society of America Bulletin 123, 1836–1850.

Korup, O., Clague, J.J., 2009. Natural hazards, extreme events, and mountain topography. Quaternary Science Reviews 28, 977–990.

Korup, O., Clague, J.J., Hermanns, R.L., Hewitt, K., Strom, A.L., Weidinger, J.T., 2007. Giant landslides, topography, and erosion. Earth and Planetary Science Letters 261, 578–589.

Lal, D., 1991. Cosmic ray labeling of erosion surfaces: in situ nuclide production rates and erosion models. Earth and Planetary Science Letters 104, 424–439.

Lifton, N.A., Bieber, J.W., Clem, J.M., Duldig, M.L., Evenson, P., Humble, J.E., Pyle, R., 2005. Addressing solar modulation and long-term uncertainties in scaling secondary cosmic rays for in situ cosmogenic nuclide applications. Earth and Planetary Science Letters 239, 140–161.

Mitchell, W.A., McSaveney, M.J., Zondervan, A., Kim, K., Dunning, S.A., Taylor, P.J., 2007. The Keylong Serai rock avalanche, NW Indian Himalaya: geomorphology and palaeoseismic implications. Landslides 4, 245–254.

Nishiizumi, K., Imamura, M., Caffee, M.W., Southon, J.R., Finkel, R.C., McAninch, J., 2007. Absolute calibration of ^{10}Be AMS standards. Nuclear Instruments and Methods in Physics Research Section B: Beam Interactions with Materials and Atoms 258, 403–413.

Owen, L.A., 1991. Mass movement deposits in the Karakoram Mountains: their sedimentary characteristics, recognition and role in Karakoram landform evolution. Zeitschrift für Geomorphologie 35, 401–424.

Owen, L.A., Kamp, U., Khattak, G.A., Harp, E.L., Keefer, D.K., Bauer, M.A., 2008. Landslides triggered by the October 8, 2005, Kashmir Earthquake. Geomorphology 94, 1–9.

Owen, L.A., Chen, J., Hedrick, K.A., Caffee, M.W., Robinson, A.C., Schoenbohm, L.M., Yuan, Z., Li, W., Imrecke, D.B., Liu, J., 2012. Quaternary glaciation of the Tashkorgan Valley, southeast Pamir. Quaternary Science Reviews 47, 56–72.

Parker, R.N., Densmore, A.L., Rosser, N.J., Michele, M., Li, Y., Huang, R., Whadcoat, S., Petley, D.N., 2011. Mass wasting triggered by the 2008 Wenchuan earthquake is greater than orogenic growth. Nature Geoscience 4, 449–452.

Robinson, A.C., Yin, A., Manning, C.E., Harrison, M.T., Zhang, S.-H., Wang, X.-F., 2004. Tectonic evolution of the northeastern Pamir: constraints from the northern portion of the Cenozoic Kongur Shan extensional system, western China. Geological Society of America Bulletin 116, 953–973.

Robinson, A.C., Yin, A., Manning, C.E., Harrison, T.M., Zhang, S.H., Wang, X.F., 2007. Cenozoic evolution of the eastern Pamir: implications for strain-accommodation mechanisms at the western end of the Himalayan–Tibetan orogen. Geological Society of America Bulletin 119, 882–896.

Robinson, A.C., Yin, A., Lovera, O., 2010. The role of footwall deformation and denudation in controlling cooling age patterns of detachment systems: an application to the Kongur Shan extensional system in the eastern Pamir, China. Tectonophysics 496, 28–43.

Robinson, A.C., Ducea, M., Lapen, T.J., 2012. Detrital zircon and isotopic constraints on the crustal architecture and tectonic evolution of the northeastern Pamir. Tectonics 31 16pp.

Seong, Y.B., Owen, L.A., Bishop, M.P., Bush, A., Clendon, P., Copland, P., Finkel, R., Kamp, U., Shroder, J.F., 2008. Rates of fluvial bedrock incision within an actively uplifting orogen: central Karakoram Mountains, northern Pakistan. Geomorphology 97, 274–286.

Seong, Y.B., Bishop, M.P., Bush, A., Clendon, P., Copland, P., Finkel, R., Kamp, U., Owen, L.A., Shroder, J.F., 2009a. Landforms and landscape evolution in the Skardu, Shigar and Braldu valleys, central Karakoram. Geomorphology 103, 251–267.

Seong, Y.B., Owen, L.A., Yi, C., Finkel, R.C., 2009b. Quaternary glaciation of Muztag Ata and Kongur Shan: evidence for glacier response to rapid climate changes throughout the Late Glacial and Holocene in westernmost Tibet. Geological Society of America Bulletin 121, 348–365.

Seong, Y.B., Owen, L.A., Yi, C., Finkel, R.C., Schoenbohm, L., 2009c. Geomorphology of anomalously high glaciated mountains at the northwestern end of Tibet: Muztag Ata and Kongur Shan. Geomorphology 103, 227–250.

Shi, Y., Yu, G., Liu, X., Li, B., Yao, T., 2001. Reconstruction of the 30–40 ka BP enhanced Indian monsoon climate based on geological records from the Tibetan Plateau. Paleogeography, Paleoclimatology, Paleoecology 169, 69–83.

Shroder Jr., J.F., Bishop, M.P., 1998. Mass movement in the Himalaya: new insights and research directions. Geomorphology 26, 13–35.

Shroder, J., Owen, L.A., Seong, Y.B., Bishop, M.P., Bush, B., Caffee, M.W., Finkel, R.C., Kamp, U., 2011. The role of mass movement on landscape evolution in the central Karakoram: discussion and speculation. Quaternary International 236, 34–47.
Shulmeister, J., Davies, T.R., Evans, D.J.A., Hyatt, O.M., Tovar, D.S., 2009. Catastrophic landslides, glacier behavior and moraine formation — a view from an active plate margin. Quaternary Science Reviews 28, 1085–1096.
Stone, J.O., 2000. Air pressure and cosmogenic isotope production. Journal of Geophysical Research 105, 23753–23759.
Sun, B., Mao, W., Feng, Y., Chang, T., Zhang, L., Zhao, L., 2006. Study on the change of air temperature, precipitation and runoff volume in the Yarkant River basin. Arid Zone Research 23, 203–209 (in Chinese with English abstract).
Yi, C., Zhu, L., Seong, Y.B., Owen, L.A., Finkel, R.C., 2006. A lateglacial rock avalanche event, Tianchi Lake, Tien Shan, Xinjiang. Quaternary International 154–155, 26–31.
Yuan, Z., Chen, J., Li, W., Owen, L.A., Schoenbohm, L.M., 2012. ^{10}Be dating of Taheman large-scale landslide in eastern Pamir and paleoseismic implications. Quaternary Science 32, 409–416 (in Chinese with English abstract).